Article

Mapping dysfunctional circuits in the frontal cortex using deep brain stimulation

Barbara Hollunder [1,2,3], Jill L. Ostrem[4], Ilkem Aysu Sahin [1,2], Nanditha Rajamani[1], Simón Oxenford [1], Konstantin Butenko[5], Clemens Neudorfer[5,6], Pablo Reinhardt[7], Patricia Zvarova[1,2], Mircea Polosan[8,9,10], Harith Akram [11,12], Matteo Vissani [6,13,14], Chencheng Zhang [15], Bomin Sun [15], Pavel Navratil[16], Martin M. Reich [16], Jens Volkmann[16], Fang-Cheng Yeh [17], Juan Carlos Baldermann[18,19], Till A. Dembek [5,19], Veerle Visser-Vandewalle [20], Eduardo Joaquim Lopes Alho[21], Paulo Roberto Franceschini[22], Pranav Nanda[6], Carsten Finke [2,3,23], Andrea A. Kühn [1,2,3,24], Darin D. Dougherty [25], R. Mark Richardson [6], Hagai Bergman [26,27,28], Mahlon R. DeLong[29], Alberto Mazzoni[13,14], Luigi M. Romito [30], Himanshu Tyagi [11,31], Ludvic Zrinzo [11,12], Eileen M. Joyce [11,31], Stephan Chabardes[8,9,32], Philip A. Starr [33], Ningfei Li [1,34] ✉ & Andreas Horn [1,2,5,6,34] ✉

Frontal circuits play a critical role in motor, cognitive and affective processing, and their dysfunction may result in a variety of brain disorders. However, exactly which frontal domains mediate which (dys)functions remains largely elusive. We studied 534 deep brain stimulation electrodes implanted to treat four different brain disorders. By analyzing which connections were modulated for optimal therapeutic response across these disorders, we segregated the frontal cortex into circuits that had become dysfunctional in each of them. Dysfunctional circuits were topographically arranged from occipital to frontal, ranging from interconnections with sensorimotor cortices in dystonia, the primary motor cortex in Tourette's syndrome, the supplementary motor area in Parkinson's disease, to ventromedial prefrontal and anterior cingulate cortices in obsessive-compulsive disorder. Our findings highlight the integration of deep brain stimulation with brain connectomics as a powerful tool to explore couplings between brain structure and functional impairments in the human brain.

Studying brain connectomics with deep brain stimulation (DBS) represents a compelling framework for identifying circuits that associate with successful neuromodulation therapy[1,2]. This potential arises from modeling structural connections activated by variably placed electrodes across patients and relating modulated connections to symptom improvements[1,3]. As a first-order approximation, effective DBS is seen to act akin to a functional lesion[4], achieving downregulation of dysfunctional networks that were involved in neurological or neuropsychiatric symptoms in the first place. By isolating circuits that exhibit the most favorable response to DBS interventions, we, hence, advance understanding of the precise brain circuits associated with dysfunctions in particular disorders[1,3]. As such, this methodology can be used to outline the human 'dysfunctome'—that is, the set of connections that are disrupted in given brain disorders—and may be tuned down by successful neuromodulation.

Disrupted interactions between the frontal cortex and basal ganglia lie at the root of numerous brain disorders. These interconnections govern motor, cognitive and affective functions[5] and are implemented as fronto-subcortical circuits that cross-communicate[6,7] but retain a certain degree of segregation at cortical, striatal, pallidal/nigral and thalamic levels[6,8]. Although the striatum has often been described as the primary input structure within the basal ganglia, the subthalamic nucleus (STN) has recently been recognized as a second direct input nucleus[9]. The STN is much smaller than the striatum (~240 mm³)[10] but similarly receives efference copies of projections from the entire frontal cortex[6]. This property renders the STN an ideal gateway for modulating large-scale brain networks through direct electrical stimulation delivered by invasive electrodes.

Indeed, targeting the same nucleus has proven an effective therapy for a heterogeneous spectrum of disorders that includes Parkinson's disease (PD)[11], dystonia (DYT)[12,13], obsessive-compulsive disorder (OCD)[14,15] and Tourette's syndrome (TS)[16,17]. At first glance, it may appear paradoxical that applying electrical stimulation to a subcortical structure of such constrained extent could alleviate symptoms in four disorders that manifest as differently from one another at a phenotypical level. However, this seeming paradox may open a unique opportunity. Because the same compact nucleus is used as a DBS target for different disorders, it acts as a network node that provides therapeutic access to malfunctioning circuits in each of these conditions. By isolating circuits whose modulation entails the most substantial treatment benefit, we may be able to disentangle whether one and the same—or, rather, multiple different—dysfunctional networks are implicated in these multiform phenotypic presentations.

Here we apply this concept by integrating 534 DBS electrodes—each implanted for treatment of DYT, PD, TS or OCD symptoms—and their corresponding clinical outcomes with detailed structural connectomes of the human brain. We analyze the dataset on both local and global network levels by applying DBS Sweet Spot Mapping[18] and DBS Fiber Filtering[19]. The resulting circuits segregate the frontal cortex and its hyperdirect and indirect pathway connections with the STN into distinct dysfunctional territories. We base this work on broad definitions of cardinal symptoms present in each of these disorders (as measured by established rating scales used in clinical practice).

Results

Patient demographics and clinical results

Discovery cohorts. Each of the four disorders was represented by two cohorts of bilaterally implanted STN-DBS patients (*n* = 197, 80 females), amounting to a total of *n* = 394 analyzed DBS electrodes: DYT (*n* = 70, 38 females), PD (*n* = 94, 29 females), OCD (*n* = 19, 10 females) and TS (*n* = 14, three females). Average improvements from DBS ON to baseline were similar between cohorts and centers. In DYT, the San Francisco cohort presented with an average improvement of 52 ± 42% and the Shanghai cohort of 65 ± 29% on the motor subscale of the Burke–Fahn–Marsden Dystonia Rating Scale (BFMDRS). Patients in the TS cohort from Pisa/Milan benefitted by 62 ± 18% and those from Shanghai by 59 ± 24% on the Yale Global Tic Severity Scale (YGTSS). In PD, Berlin patients improved by 45 ± 23% and the Würzburg cohort by 49 ± 24% on the Unified Parkinson's Disease Rating Scale–Part III (UPDRS-III). DBS entailed a 45 ± 29% reduction within the Yale-Brown Obsessive-Compulsive Scale (Y-BOCS) for the OCD cohort from London after 'STN-DBS-only' stimulation, and Grenoble patients improved by 44 ± 32%. A comprehensive summary of demographic and clinical patient characteristics along with DBS and imaging specifications is provided in Supplementary Table 1. Supplementary Tables 2–5 provide detailed patient-specific information. Figure 1 recapitulates applied methodological concepts in graphical form. Electrode localization confirmed electrode placement within the subthalamic region in all patients (Fig. 2).

Validation cohorts. Validation of the PD streamline model was based on an additional STN-DBS cohort (*n* = 32, 10 females) from Würzburg, characterized by a mean reduction of 47 ± 21% on the UPDRS-III. In OCD, an additional patient cohort (*n* = 35, 18 females) receiving DBS to the ventral capsule/ventral striatum (VC/VS) region was pooled across Cologne, Boston and London centers. Critically, electrodes of these novel cohorts were entirely independent from those used to create the streamline models (see Methods for the special case of London patients). On average, Cologne patients benefitted from DBS by 31 ± 21%, those from London after 'VC/VS-DBS only' by 53 ± 26% and those from Boston by 40 ± 30% on the Y-BOCS. Additional cohort-averaged specifics are featured in Supplementary Table 6, with patient-wise information in Supplementary Table 7 (PD validation cohort) and Supplementary Table 8 (OCD validation cohorts).

Finally, two DBS patients (one with PD and OCD each) were prospectively reprogrammed, and one OCD patient was prospectively implanted and programmed as informed on the streamline models established here (see below for more detailed case vignettes).

Dysfunction mappings at the subthalamic level

Model definition. Disease-wise stimulation effects were mapped into anatomical space at the subthalamic level. A caudo-rostral latero-medial organization emerged for peak voxels associated with beneficial stimulation ranging from DYT to TS, PD and OCD (Fig. 3, center). This result was consistent with functional zones commonly associated with anatomical portions of the nucleus (DYT in the sensorimotor, TS in the motor, PD in the motor-premotor and OCD in the associative-limbic domain). A detailed overview of the anatomical localization of sweet and sour spots for each disease is provided in Fig. 3 (top and bottom panels). Peak voxel coordinates are reported in Supplementary Table 9.

Estimation of outcomes based on the model. Spatial correlations between electric fields (E-fields) and the optimal pattern were performed to confirm that the sweet spot model could explain variance in clinical outcomes (Fig. 3, middle panel, left and right). This analysis was carried out (1) to compare results between disorders and (2) to compare amounts of variance accounted for by sweet spots versus sweet streamlines. Critically, these in-sample analyses were circular in nature and should, thus, not be overinterpreted. To account for this limitation, analyses were subjected to fivefold cross-validation (CV) (Fig. 3, middle panel, left and right) to investigate generalizability of findings, which yielded significant results in all disorders but TS (with the lowest *n*). To demonstrate stability of sweet spot configurations and fivefold CVs across different E-field thresholds, we repeated the procedure with varying thresholds, which led to consistent results (Supplementary Fig. 1).

Dysfunction mappings at streamline and cortical levels

Model definition. Second, we mapped optimal stimulation effects to the fronto-subcortical circuitry. Disease-specific data associated different sets of streamlines with optimal symptom improvements (Figs. 4a and 5). Peaks of beneficial DBS networks for DYT primarily interconnected with somatosensory (S1) and primary motor (M1) cortices. Electrode connectivity with M1 and supplementary motor areas (SMAs) emerged as most critical for high stimulation benefit in TS, with premotor regions and SMAs in PD, and with ventromedial prefrontal, dorsal anterior cingulate, dorsolateral prefrontal and orbitofrontal cortices in OCD. Supplementary Fig. 2 displays rotated views of these streamline segregations. Peak voxel coordinates of interconnected cortical sites are summarized in Supplementary Table 9.

Although we consider the visualization of thresholded peaks as most meaningful, thresholding may also mask weaker local optima. Supplementary Fig. 3 provides more comprehensive, unthresholded landscapes of streamlines. Moreover, we quantified statistical certainty per streamline (defined by the −log(*P*) value) to visualize
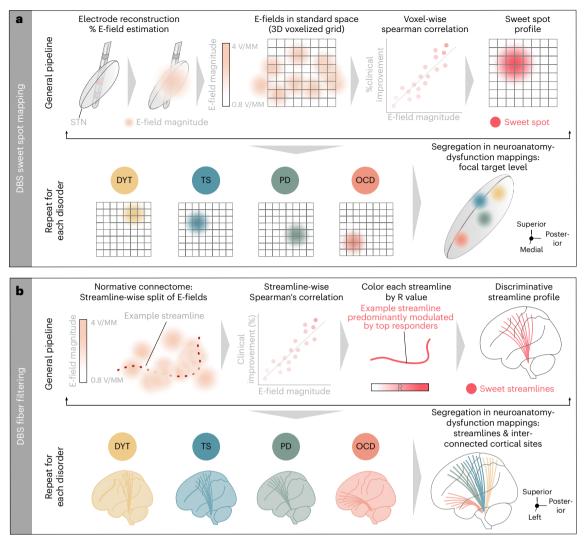
Fig. 1 | Overview of the twofold group-level approach of (sub)cortical dysfunction mapping. a, DBS Sweet Spot Mapping[18]. Patient-specific electrode reconstructions were first derived relative to their precise position within the STN region and integrated with individual stimulation parameters to estimate E-field magnitudes. Subsequently, Spearman's rank correlations between E-field magnitudes and clinical improvements were performed (separately for each disease). Applying this procedure across voxels resulted in a detailed grid of positively (sweet spot) and negatively (sour spot, not shown here) associated stimulation sites. **b**, DBS Fiber Filtering[19]. Each streamline within a predefined normative connectome was weighted by its ability to discern good from poor responders in each respective cohort. To do so, the peak E-field magnitudes among samples drawn along the course of each streamline were Spearman's rank correlated with clinical outcomes. Streamlines predominantly modulated by high E-field magnitudes of good responders received high positive weights (sweet streamlines), whereas those associated with high E-field magnitudes of poor responders were attributed high negative weights (sour streamlines, not represented here).

the influence of smaller sample sizes on mappings (Supplementary Fig. 4). As expected, this revealed the lowest certainty for the TS cohort (which had the smallest sample size).

Influence of electrode placement. Notably, DBS Fiber Filtering results describe streamlines associated with clinical improvements, which should not be confused with mere electrode connectivity. Indeed, mean implantation sites of the standard (second-to-lowest) DBS contact in DYT, PD and TS resided at negligible distance from each other along the y axis of the STN (P of all independent two-sample t-test comparisons > 0.27, two-sided tests), whereas a significantly different subthalamic aspect was targeted in OCD (all P < 0.01, two-sided tests). Hence, we hypothesized the organization of dysfunction mappings to predominantly reflect the stimulation impact on different symptoms rather than mere differences in electrode placement (at least in all disorders but OCD).

To test this assumption further in a data-driven fashion, we implemented a total of three control analyses. First, from the entirety of plain electrode connections per disorder (Fig. 4a, top row), we isolated the subset common to all four disorders and compared it to disease-specific streamline models. Both four-sample and pairwise tests of equality of proportions (two-sided tests) suggested significant differences between proportions of overlap between shared and disease-specific streamlines (Supplementary Table 10).

Second, we mapped sweet spots as three-dimensional Gaussian distributions that were fit to the standard electrode contacts (second-to-lowest) across patients in each disorder. When seeding streamlines from these Gaussians, the resulting streamline profiles expectedly looked much less segregated than the dysfunction mappings achieved by DBS Fiber Filtering. Although, as anticipated, a slight segregation of the OCD bundle emerged given significantly different placement, streamlines seeding from the Gaussians of other disorders
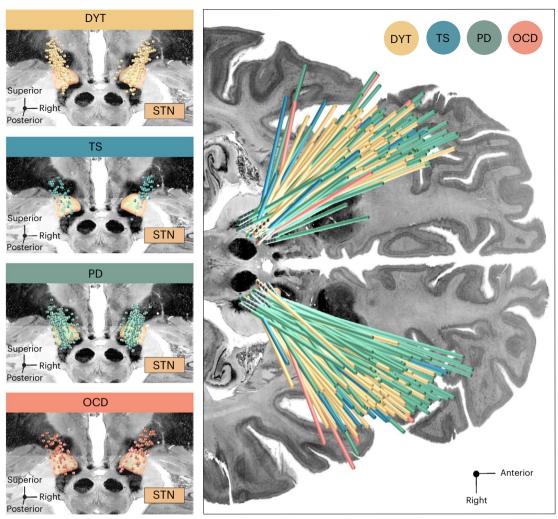
Fig. 2 | Overview of electrode placements relative to the STN across discovery cohorts. Left panels, DBS electrode placement is shown in relation to a posterior view of the STN in DYT ($n = 56$), PD ($n = 94$), TS ($n = 14$) and OCD ($n = 19$) cohorts, respectively. Electrode contacts are visualized as point clouds. Right panel, visualization of DBS leads of the four discovery cohorts investigated in the present study are featured in the axial plane and colored according to indication. The STN is defined by the DISTAL atlas, version 1.1 (ref. 28), with an axial plane of the BigBrain template in 100-µm resolution[66] displayed as a backdrop ($y = -5$ mm, $z = -10$ mm).

were indistinguishable. Furthermore, the OCD streamline bundle was by far not as anteriorly located as in the model that was driven by clinical improvements (Supplementary Fig. 5).

In a final control analysis, we color-coded therapeutic streamlines by a dedicated specificity value. This value was calculated by dividing each streamline's R value by the average of the R values it had been tagged by within the remaining disorder-specific models. The resulting partitioning among disease-specific streamline bundles highly resembled the one achieved by our 'conventional' mapping approach (Supplementary Fig. 6), underlining specificity of dysfunction attributions.

Estimation of outcomes based on the model. Using E-field overlap with optimal streamline profiles to estimate clinical improvements of individual patients based on a (circular) in-sample design resulted in significant correlations for all disorders (Fig. 4b). When subjected to fivefold CVs, DYT and PD models were robust across all connectomes but less so for disorders comprising smaller sample sizes (TS and OCD) (Fig. 4b). This is not surprising, because fivefold CVs for models calculated on 14 (TS) or 19 (OCD) patients are prone to failure, by design. Robustness of findings from the larger cohorts, however, make us confident about the general validity of methodological choices. Furthermore, the OCD response bundle identified here has been widely

reproduced based on OCD cohorts stimulated to the STN and other subcortical targets (see ref. 20 for a review).

Model specificity. Despite discernible segregation in dysfunction mappings, disease-wise streamline models, expectedly, also showed considerable overlaps, most visibly among DYT and TS. To quantify the degree of specificity, each profile was, hence, used to cross-estimate outcomes in all remaining disorders. At large, streamline models explained significant amounts of variance uniquely in the disease for which they had initially been calculated (Supplementary Fig. 7).

Influence of connectome. Main analyses were informed on a group connectome[21] calculated on diffusion-weighted magnetic resonance imaging (dMRI)-based tractography of 985 healthy participants of the Human Connectome Project (HCP)[22]. Although representative of average/population brain connectivity, the choice of this particular connectome may bias results. We, thus, repeated our DBS Fiber Filtering analyses using five additional normative connectomes. First, we implemented a connectome of unprecedented spatial (760 µm) and angular resolution based on a single healthy human brain[23], which optimally lends itself for the detailed visualization of dysfunction mappings (Supplementary Fig. 8b).
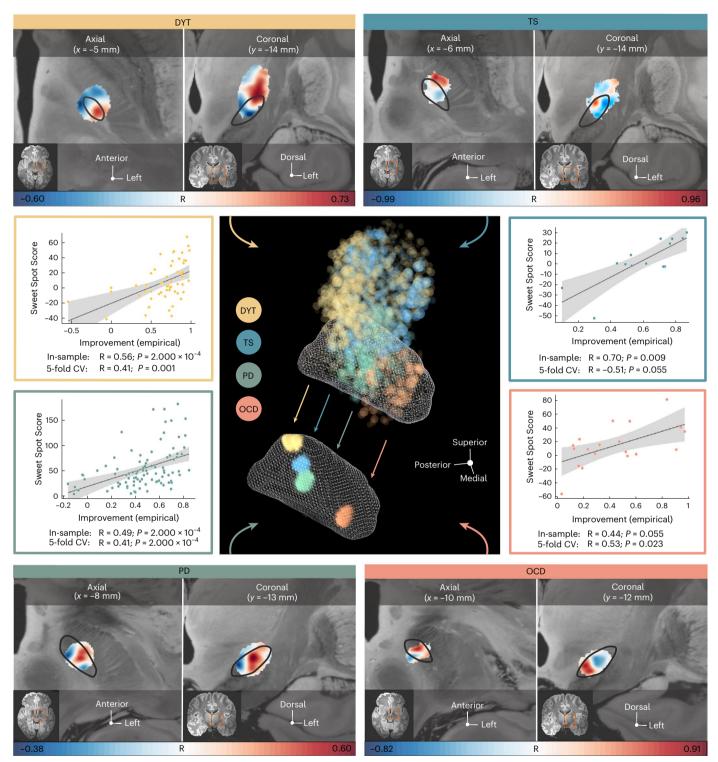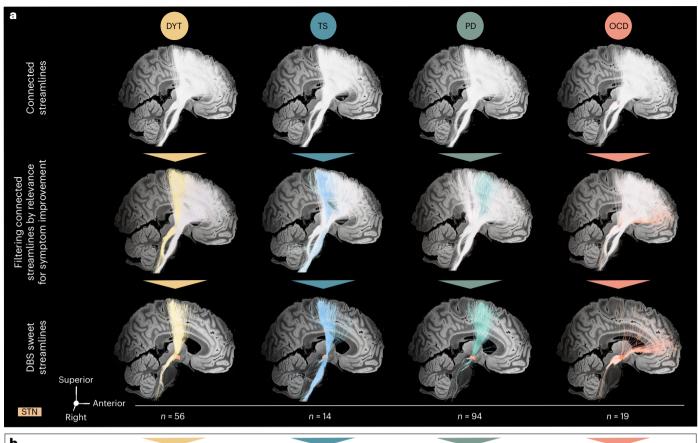
Fig. 3 | Segregation of dysfunction mappings at the subthalamic level by disease-specific stimulation effects. Middle panel (center), the topographical organization of disorder-specific DBS sweet spots in DYT ($n = 56$), TS ($n = 14$), PD ($n = 94$) and OCD ($n = 19$) is shown as a density cloud plot relative to a three-dimensional model of the left STN in template space derived from the DISTAL atlas, version 1.1 (ref. 28). Sphere size and transparency indicate Spearman's rank correlation strength between stimulation impact and clinical improvements at a given coordinate, with bigger and less transparent spheres coding for higher correlations. Below, binarized and thresholded sweet spot peaks are projected onto the STN surface. Top and bottom panels, axial and coronal views of sweet and sour spots are displayed relative to the left STN (black outlines), independently for each disorder, superimposed onto a 100-μm ex vivo brain template[67]. Voxels are color-coded by degree of Spearman's rank correlation (warm colors for positive associations and cool colors for negative associations) between E-field magnitudes and clinical improvements. Middle panel (left and right), Spearman's correlation plots show amounts of clinical outcome variance explained by spatial similarity of E-field peaks with disease-wise sweet spot models (expressed as Sweet Spot Score under each E-field, averaged for bilateral scores per patient) across the cohort (two-sided tests). Gray shaded areas are representative of 95% confidence intervals.
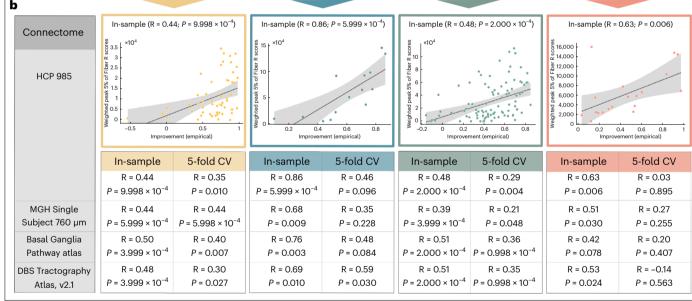
Fig. 4 | Disease-specific sweet streamline models in each discovery cohort.
a, Sweet streamlines in DYT (n = 56; peak R = 0.36), PD (n = 94; peak R = 0.37), TS (n = 14; peak R = 0.73) and OCD (n = 19; peak R = 0.49) associated with beneficial stimulation outcomes were filtered from a population-based group connectome[21]. The top row demonstrates the set of connections (in white) seeding from stimulation volumes across patients in each of the four disorders. Among these plain connections, only those were isolated via DBS Fiber Filtering (middle row) whose modulation was Spearman's rank correlated with clinical outcomes (bottom row). Sweet streamlines are highlighted in disease-specific color and displayed in thresholded and binarized fashion. Results are shown against a sagittal slice (x = −5 mm) of the 7T MRI ex vivo 100-µm human brain

template[67], in conjunction with a three-dimensional model of the right STN in template space from the DISTAL atlas, version 1.1 (ref. 28). **b**, In-sample correlations and fivefold CVs are reported for models informed on four different normative connectomes. Plots in the top row represent the fitting of a linear model to determine the degree to which the overlap of E-field magnitudes with selected HCP 985 Connectome[21] sweet streamlines explains variance in empirical clinical outcome across the cohort, as calculated using Spearman's correlation (two-sided tests). The magnitude of E-field overlap with sweet streamline models in this analysis is expressed as weighted peak 5% of Fiber R scores under each E-field, averaged across bilateral scores per patient. Gray shaded areas indicate 95% confidence intervals.
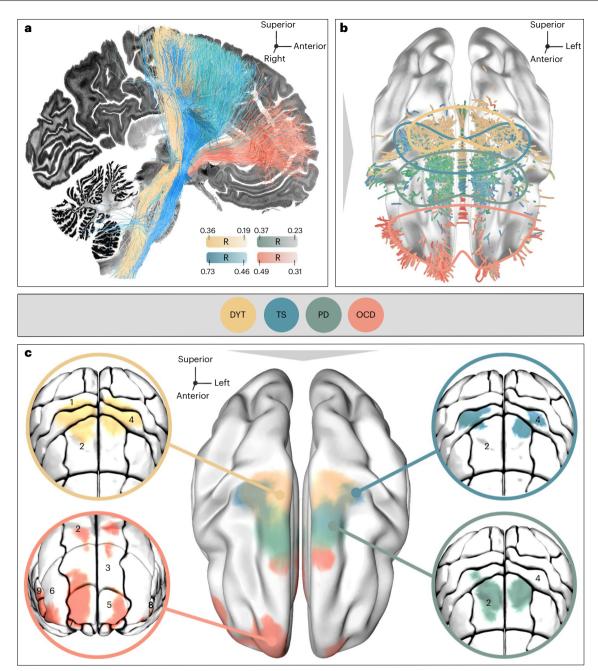
Fig. 5 | Topography of streamlines and interconnected cortical sites associated with therapeutic stimulation effects. a, Segregation into therapeutic networks is achieved by means of DBS Fiber Filtering in DYT (*n* = 56), PD (*n* = 94), TS (*n* = 14) and OCD (*n* = 19). Disease-specific optimal streamlines were isolated from a high-resolution normative group connectome[21] through association with clinical effects in each disorder. This was achieved using Spearman's rank correlation between peak E-field magnitudes by which each streamline was modulated and clinical improvements across the cohort. Mappings are displayed in thresholded form, against a sagittal slice (*x* = −5 mm) of a brain cytoarchitecture atlas in ICBM 2009b Nonlinear Asymmetric ('MNI') space[66]. Streamline color intensity is representative of R value magnitude, with darker colors corresponding to higher correlations. **b**, The same streamlines are shown in conjunction with a transparent brain in template space along with delineations that are color-coded by disease. **c**, To derive the cortical topography of dysfunction mappings, smoothed, thresholded and binarized density maps of sweet streamlines were projected onto a brain template in MNI space. Circles show close-up views of disease-wise interconnected cortical sites, anatomically characterized based on the JHU atlas parcellation[68]. Legend of relevant regions, with corresponding JHU atlas denominators in brackets: 1 (JHU: 23 and 24), postcentral gyrus; 2 (1 and 2), superior frontal gyrus (posterior segment); 3 (3 and 4), superior frontal gyrus (prefrontal cortex); 4 (25 and 26), precentral gyrus; 5 (5 and 6), superior frontal gyrus (frontal pole); 6 (9 and 10), middle frontal gyrus (dorsal prefrontal cortex); 7 (17 and 18), lateral fronto-orbital gyrus; 8 (13 and 14), inferior frontal gyrus pars orbitalis; 9 (15 and 16), inferior frontal gyrus pars triangularis.

A key problem of data-driven whole-brain connectomes (as the two mentioned above), however, is their proneness to false-positive stream-lines[24] and low accuracy in representing small subcortical tracts[25]. To account for this, we repeated our analysis based on a pathway atlas manually curated by expert anatomists[26] (Supplementary Fig. 8c). Although this dataset is likely the most accurate atlas of subcortical streamlines that currently exists, a potential drawback lies in its proneness to false negatives (because not all fibers of the brain were
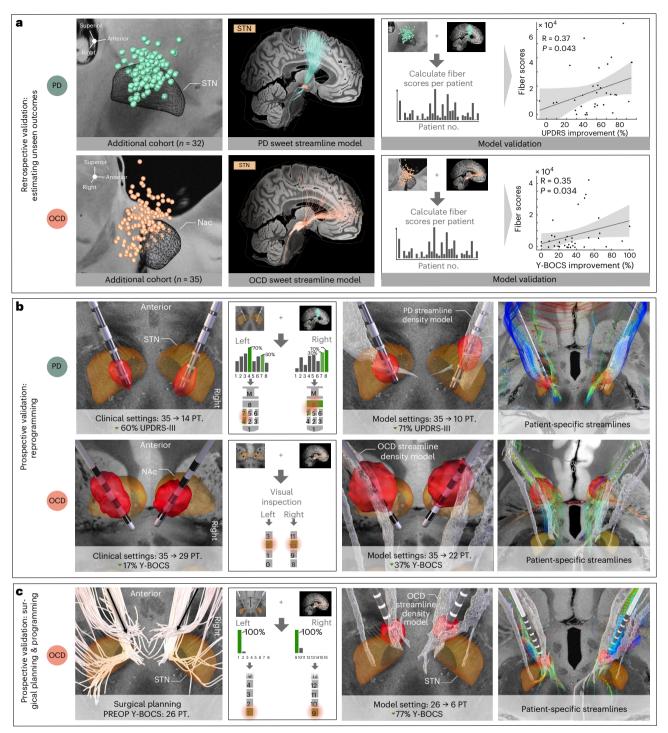
Fig. 6 | Retrospective and prospective validations of therapeutic streamline targets. To probe the validity of PD and OCD streamline models, five validation experiments were carried out. **a**, First and second, empirical outcomes of two additional independent datasets (PD: $n = 32$ and OCD: $n = 35$) could significantly be estimated based on the degree of overlap of their stimulation volumes with the streamline models. Sweet streamline models calculated on discovery cohorts are represented in disease-specific color, in thresholded and binarized fashion. Model validity is expressed in the form of Spearman's correlations between the stimulation magnitude by which positive streamlines in the model were respectively modulated (weighted peak 5% of Fiber R scores attributed to each E-field, averaged for bilateral scores per patient) and empirical clinical improvements across the cohort (two-sided tests). Gray shaded areas represent 95% confidence intervals. **b**, Third and fourth, prospective reprogramming was undertaken in two patients. In the patient with PD, directional electrodes had been implanted, so the current

was divided using a 70/30% rule based on the contacts with the strongest and second-to-strongest streamline overlaps. This led to an improvement of 71% on the UPDRS-III compared to 60% using clinical settings. In the OCD case, the contact was selected based on visual inspection with the streamline model by the clinical team. This led to a reduction of 37% on the Y-BOCS compared to 17% under clinician-selected parameters. **c**, Fifth, a prospective OCD case underwent streamline-guided DBS surgery. Electrodes were activated at the contact with the highest streamline overlaps (most ventral contacts bilaterally), leading to a rapid Y-BOCS reduction of 77% already 1 month after surgery. Depending on the respective target, reconstructed electrodes and stimulation volumes are featured relative to three-dimensional models of the STN from the DISTAL atlas, version 1.1 (ref. 28), or of the nucleus accumbens (Nac) from the California Institute of Technology reinforcement learning (CIT168) atlas, version 1.1 (ref. 69), and against anatomical slices of a 100-μm ex vivo brain template[67]. PREOP, pre-operative; PT., points.
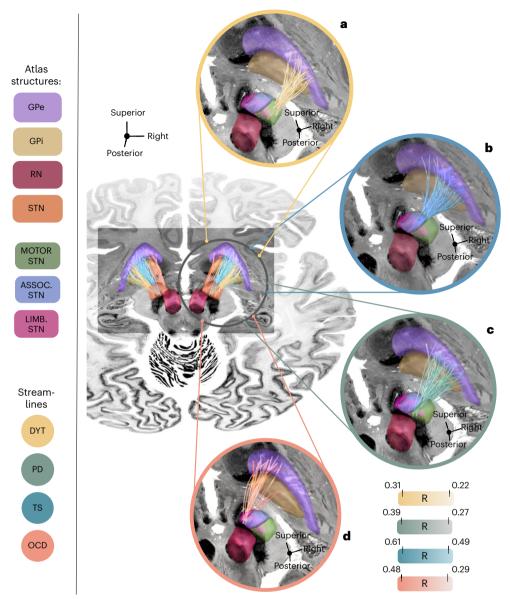
Fig. 7 | Conserved segregation of dysfunction mappings among indirect pallido-subthalamic connections. Disease-wise sweet streamlines retain a high degree of specificity along their indirect pathway trajectory connecting the STN with the GPi and GPe. Connectivity is modeled based on the Basal Ganglia Pathway Atlas[26]. Sweet streamlines associated with optimal DBS outcomes in DYT ($n = 56$) are interconnected with sensorimotor (**a**), in TS ($n = 14$) with associative (**b**), in PD ($n = 94$) with premotor (**c**) and in OCD ($n = 19$) with limbic (**d**) STN territories. Streamlines are thresholded and represented in disease-specific color. Color intensities attributed to each streamline code for the degree of Spearman's rank correlation between streamline modulation (peak E-field magnitudes) and clinical outcomes across the disease cohort, with darker colors indicative of higher correlations. Results are displayed relative to several anatomical structures from the DISTAL atlas, version 1.1 (ref. 28), and in conjunction with an axial slice ($z = -10$ mm) of the BigBrain template[66]. ASSOC. STN, associative territory of the STN; LIMB. STN, limbic territory of the STN; MOTOR STN, motor territory of the STN; RN, red nucleus.

delineated in this resource). Second, as the atlas is not based on empirical dMRI, small details of streamline trajectories in template space may be misaligned. Thus, we additionally replicated analyses using a pathway atlas informed on population-based fiber tracking combined with expert-defined pathways[26,27], which we amended with interconnections between the STN and the entire frontal cortex (DBS Tractography Atlas, version 2.1; Supplementary Fig. 8d).

Finally, the generalizability of dysfunction mappings based on normative connectomes to disease-specific alterations remains uncertain. In view of potential therapeutic implications of the identified mappings, we, thus, repeated our DBS Fiber Filtering approach in two exemplary disease-matched group connectomes—one informed on diffusion scans of six patients with OCD (Supplementary Fig. 9a) and

one on those of 85 patients with PD[28] (Supplementary Fig. 9b). A similar rostro-occipital organization emerged across connectomes, with the same order of motor disorders in sensorimotor and premotor cortices toward associative-limbic OCD connections. In-sample correlations and fivefold CVs based on normative and disease-matched connectome models are reported in Fig. 4b and Supplementary Fig. 9c, respectively.

Retrospective and prospective streamline model validations

Given the potential clinical-translational relevance of identified streamlines in guiding treatment for optimized benefit, we carried out a total of five validation experiments in independent data. We focused on PD and OCD as two substantially distinct brain circuit disorders, because additional retrospective cohorts were unavailable in the remaining

two disorders, and no prospective enrollments of patients with these conditions took place at centers associated with this study. First and second, overlaps of stimulation volumes with the respective streamline model (PD or OCD) were used to estimate outcomes in two additional retrospective cohorts. In both the STN-DBS validation patients with PD (R = 0.37, P = 0.043) and the VC/VS-DBS validation cohort with OCD (R = 0.35, P = 0.034), this procedure corroborated a good fit between estimates and empirical outcomes (Fig. 6a).

Third and fourth, we reprogrammed two individual patients at Würzburg (PD) and Boston (OCD) centers with the intention of maximizing engagement of stimulation volumes with the respective streamline model (Fig. 6b). The first case was a 67-year-old male patient with 9 years into an akinetic-rigid type PD diagnosis who had been implanted to the STN with directional leads. Three months post-operatively, his score of 35 on the UPDRS-III under DBS OFF improved to 14 points (60% reduction) under clinical DBS ON (with medication OFF in both cases). Under streamline-based parameters, symptoms further reduced to 10 points (71% reduction).

The second reprogramming patient from Boston was a 21-year-old female with severe, treatment-resistant OCD characterized by obsessions about food and water intake along with compulsions involving ingestion events and skin picking. Implantation of a conventional omnidirectional lead targeting the VC/VS region led to an improvement of six points (17%) on the Y-BOCS, from 35 points (pre-surgical baseline) to 29 points post-operatively, under clinical stimulation parameters. One month after streamline-based reprogramming, this score further reduced to 22 points (37% reduction).

Fifth, we surgically implanted a pair of subthalamic electrodes for treatment of a 32-year-old male, who had suffered from refractory OCD since the age of 18 years, at the São Paulo center (Fig. 6c). After a depressive phase, the patient had developed a compulsion of noting every word novel to him and transcribing its meaning from dictionaries, by which he filled numerous notebooks. Later, he began experiencing intrusive death-related thoughts that eventually provoked compulsive religious rituals along with concomitant apathy and depression. Since according to the surgical plan, electrode localization had revealed by far the highest overlaps of the ventral-most contacts with the streamline density image; these were activated unipolarly at 3 mA per hemisphere. Only 4 weeks after surgery, the patient, as well as his caregivers, reported a marked improvement of symptoms that had been notable within 1 d after switching on the DBS system. The Y-BOCS score had improved to six points, from a pre-surgical baseline of 26 points (77% reduction).

In all three prospective cases, patient-specific tractography confirmed agreement between individual streamlines and normative models (right-most panels in Fig. 6b,c). Supplementary Table 11 summarizes these prospective patient cases.

Dysfunction mappings at the level of indirect pathways

Although hyperdirect cortico-subthalamic interconnections are best suited to segregate the frontal cortex, the cortico-basal ganglia-thalamocortical system forms loops that include indirect projections from the striatopallidofugal system (and particularly the external pallidum (GPe)) to the STN[29]. Structural representations of the indirect pathway connecting GPe and STN are organized within Edinger's comb system[18,30] and difficult, if not impossible, to reconstruct from diffusion imaging given their orthogonal course to the highly anisotropic internal capsule[26].

To interrogate the topography of dysfunction attributions at the level of indirect connections, we, thus, repeated our DBS Fiber Filtering analysis based on pallido-subthalamic streamlines provided by the Basal Ganglia Pathway Atlas[26]. Again, segregation was evident between disease-wise interconnected sites, and their anatomical organization was largely consistent with the one of hyperdirect pathway and sweet spot mappings (Fig. 7). Therapeutic indirect connections in DYT were

interconnected with sensory/sensorimotor regions of the STN, whereas those in PD connected to territories within the premotor zone of the nucleus. Interconnected sites in TS predominantly resided within associative aspects and those of OCD within limbic subthalamic areas (insets in Fig. 7).

Discussion

Derived from 534 invasive brain stimulation sites spanning 11 patient cohorts and three prospective patient cases treated for DYT, TS, PD or OCD across 10 international institutions, we draw three key conclusions. First, we showcase the network effects of intracranial brain stimulation as a viable tool for systematically investigating the coupling between circumscribed cortical circuits and selective clinical dysfunctions. As a method, this approach is capable of mapping what we term the human 'dysfunctome'—that is, the sets of connections that are disrupted and malfunctioning across different brain disorders. Second, we demonstrate the topographical organization of dysfunction mappings to be mirrored across neuroanatomical levels: (1) among prefronto-subthalamic loops and interconnected cortical sites, (2) within pallido-subthalamic connections and, in miniaturized fashion, (3) within subthalamic subterritories. Dysfunctional networks primarily interconnected the STN with sensorimotor and cerebellar cortices in DYT while involving M1 and SMAs in TS, premotor and supplementary motor areas in PD and ventromedial prefrontal, anterior cingulate, dorsolateral prefrontal and orbitofrontal cortices in OCD. Third, by their association with previous treatment success, these attributions may hold clinical significance as therapeutic targets in stereotactic neurosurgery and non-invasive neuromodulation[1,3]. We present initial retrospective and prospective evidence of applying these results to inform clinical decision-making. Notably, we leveraged the identified circuits to improve treatment benefit in three prospective patient cases.

Methodologically, our study demonstrates the use of subcortical neuromodulation with connectomics as an effective strategy for probing relationships between neuroanatomy and functional impairments. This concept could be perceived as a network-based extension of historical studies that topographically mapped the sites of direct electrical stimulation (often applied cortically during epilepsy surgery) to specific symptoms. Among the most influential authors, Penfield and the scientific team around him assembled an exhaustive functional map of the cortex based on intraoperative mappings of sensorimotor phenomena[31]. The present paper applies a paradigm that may be perceived as a derivative of Penfield's work, combining brain stimulation administered to a specific small (but widely connected) nucleus deep inside the brain with connectomics. Demonstrating the utility of this approach could pave the way to similar work involving other subcortical and cortical neuromodulation sites. Its application at scale and in an increasingly fine-grained manner (for example, by investigating specific symptoms) may lead to more comprehensive definitions of the human 'dysfunctome'.

Conceptually, our results identify roles of cortico-basal ganglia pathways in different brain dysfunctions using an invasive method[2]. Attributions were specific to the predominant functional impairment in each disorder. Moreover, they did not reflect merely brain connections of differentially placed electrodes but also their relevance for successful symptom treatment. They were further evident irrespective of which healthy or disease-matched connectomes they had been calculated from. Before the teams at Ann Arbor and Johns Hopkins presented their work on what is now referred to as the Albin–DeLong model[32,33], the basal ganglia were conceptualized as a funnel that integrates information from different cortical strands to the motor cortex, which then initiates action. In essence, the basal ganglia had primarily been categorized as motor structures. Work by Alexander et al.[8] challenged this traditional understanding, proposing the idea of parallel circuits involving motor, cognitive and limbic processing. Although there is strong cross-communication at least on cortico-cortical,

cortico-striatal, striato-nigral and thalamo-cortical levels, loops associated with different functions retain a degree of segregation throughout their cortico-basal ganglia-thalamo-cortical course[8,34,35].

The concept of the 'hyperdirect pathway' builds on this framework, proposing that certain cortical neurons send direct projections to the STN, which bypass the striatum to create a direct link between the cortex and the structure[6,36]. The functional grouping of subthalamic terminals within these hyperdirect projections can be best understood based on their cortical origins. In this vein, a dorsolateral motor aspect comprising connections to M1 and SMA is defined, along with a ventromedial cognitive territory with origin in superior, middle and inferior prefrontal cortices, and a limbic anteromedial tip connected with orbitofrontal, anterior cingulate and ventromedial prefrontal cortices, hippocampus and amygdala[5,6]. The present results substantiate the general pattern of this distribution based on invasive stimulation sites in four different brain disorders.

Despite confirming a certain amount of segregation between loops, our findings are also compatible with the concept of cross-communication or integration as well as so-called open-loop architectures[6,7]. Indeed, therapeutic targets identified here showed considerable overlaps (most notably between DYT and TS; also see Supplementary Fig. 3). In line with the concept of 'processing gradients' (rather than entirely segregated loops), our analysis demonstrates preferential mappings between neuroanatomy and stimulation effects. This notion fits with evidence on partial convergence between terminals from different cortical projection sites and interaction between functional subthalamic subterritories[6].

Clinically, the identified circuits directly represent therapeutic targets that could inform stereotactic targeting in neurosurgery and potentially non-invasive neuromodulation at the cortical level[1]. This is underscored by the successful retrospective and prospective validations of the OCD and PD streamline targets in the present study, which provide initial evidence for clinical applications of our findings. We must emphasize, however, that the degree of certainty varies between the studied disorders as a function of the sizes of available samples, especially in TS as a relatively novel application for subthalamic DBS with only few implantations performed worldwide.

Sensorimotor and cerebellar loops have been linked to symptom improvements in DYT by investigations that used similar sources of information (such as lesions or different forms of brain stimulation)[18,37]. The sensorimotor cortex along with its basal ganglia interconnections[38], but also the cerebellum and cerebello-thalamic pathway[39,40], have been related to dystonic pathophysiology, with non-invasive sensorimotor-cortical[41] as well as cerebellar[42] stimulation yielding clinical benefit. Under DBS, aspects of motor control, such as motor sequence learning, voluntary movement coordination, sensorimotor adaptation and the control of specific body parts, may improve, which depend on the accurate functioning of cerebellar or sensorimotor loops (or an integration of both)[43].

In PD, fronto-subthalamic loops connecting the SMA to the STN have been deemed critical in both historical[44] and recent work[45,46]. Structural connectivity between subthalamic electrodes and SMA as well as pre-motor areas correlated with motor improvements in PD, and overlap of stimulation volumes with this set of streamlines, was associated with outcomes in independent patients[45]. This is in line with PD motor benefit observed under cortical SMA stimulation[47]. Functionally, these therapeutic effects may relate to involvement of the SMA in movement selection, preparation and initiation[48].

The streamline bundle identified in the OCD cohort emerged as an effective 'OCD response streamline target' beyond stimulation of the STN region (for a review, see ref. 20). Conceptualized as an associative-limbic hyperdirect pathway with passage through the internal capsule on its trajectory toward the STN and other mesencephalic nuclei, this bundle is connected to diverse prefronto-cortical regions, such as the anterior cingulate and dorsolateral prefrontal cortex[5,6].

These findings were also confirmed via functional mappings[20,49]. Concurrently, these cortical sites have been FDA approved as transcranial neuromodulation targets for OCD[50]. Functionally, recalibrating this streamline bundle may resolve repetitive thoughts and behavior by interrupting a pathological control signal emitted through hyperactive prefrontal regions[20].

Network correlates to restore functionality in TS are less established, especially not via the more recent application of subthalamic DBS[16,17]. Here, the most highly weighted hyperdirect streamlines showed connectivity to M1 and SMA. These regions align with tic-related alterations[51,52], have been associated with tic reduction under thalamic[53] or pallidal DBS[54,55] and have been probed as non-invasive neuromodulation targets for TS[56]. The SMA, in interaction with M1, may be involved in tic preparation, relaying signals to areas underpinning action monitoring or tic execution[57].

Our study has several limitations. First, analyses relied mainly on retrospective data, which may bias the interpretation of clinical outcomes. Aggregation of a large multi-center sample ($n = 534$ electrodes) further inevitably introduced different sources of variability. Still, most of our models extrapolated across differences in targeting strategies between surgeons and centers, imaging modalities and protocols, electrode models, stimulation paradigms or clinical assessment strategies. Furthermore, we validated results on unseen cohorts and prospectively tested PD and OCD circuits in individual patient cases.

Second, the underlying physiological effect may not be fully captured by the simplified biophysical model employed here to approximate the amount of tissue activated. For instance, E-field models neglect the impact of stimulation onto glial cells, intracellular processes or synaptic reorganization[58]. In addition, varying stimulation parameters may entail differential consequences[59]. For these reasons, refined modeling of the focal stimulation impact might contribute to a further increased validity of results[25].

Third, warping lead localizations into template space may have introduced slight mismatches. We sought to counteract this bias as much as possible by using an advanced processing pipeline that included brain shift correction[60], multi-spectral normalization, subcortical refinements and phantom-validated electrode reconstructions[61]. We further applied a normalization strategy with similar performance in STN segmentation as manual delineations by anatomical experts in two independent evaluations[62,63]. In addition to meticulous visual inspection and refinement of all remaining outputs of this processing pipeline, the subthalamic atlas fit was manually optimized via the WarpDrive toolbox[64].

Fourth, with patient-specific dMRI largely unavailable, anatomical delineations were based on normative or disease-matched connectivity. Undoubtedly, the use of connectivity acquired outside of the patient sample in question introduces limitations regarding the anatomical accuracy. Nevertheless, an advantage of normative connectomes lies in their higher resolution and signal-to-noise ratio than what would be attainable during clinical routine. This unprecedented quality results from the possibility of longer scanning durations and reduced movement artifacts in healthy participants as compared to movement disorder and neuropsychiatric patient populations. Similarly, the frequent use of advanced acquisition tools critically contributes to increased imaging quality. At the same time, our study was precisely aimed at deriving a 'broad lens' description of dysfunctional networks in the average human brain, and mappings were largely consistent across four normative connectomes. Additionally, we demonstrated the validity of segregations in the face of disease-specific connectivity alterations. Although here and in previous research (for a review, see ref. 1) normative models could significantly account for variance in clinical outcome outside of the discovery sample and showed prospective clinical benefit, the reported streamlines should be further validated in patient-specific data before clinical application in stereotactic targeting and programming of DBS systems.

Finally, cohorts of two disorders (OCD and TS) analyzed in the present study were similarly small, and most of the resulting models did not survive CVs. The same methodology was applied to all disorders, and, hence, the approach itself could be validated based on the remaining two disorders (PD and DYT). We further validated the OCD streamline model using an additional patient cohort and two prospective cases. Concurrently, the same bundle has been described[21,65] and validated repeatedly in earlier work to be relevant for OCD (for a review, see ref. 20). However, especially for TS, the limitation of a low *n* still stands.

In conclusion, our study demonstrates the potential of invasive brain stimulation as a 'flashlight' pointing from the subcortex onto the topography of the human 'dysfunctome'. Specifically, we found beneficial stimulation effects in four different brain disorders to be organized as a function of cardinal symptom domain at the level of fronto-subthalamic circuits and their interconnected cortical sites. Intriguingly, a comparable—yet miniaturized—topography was mirrored focally at the site of stimulation in the subcortex. This scaling effect on dysfunction attributions across neuroanatomical levels provides a compelling answer to the conundrum of similar clinical effects after stimulation to different access nodes of a shared therapeutic network.

Online content

Any methods, additional references, Nature Portfolio reporting summaries, source data, extended data, supplementary information, acknowledgements, peer review information; details of author contributions and competing interests; and statements of data and code availability are available at https://doi.org/10.1038/s41593-024-01570-1.

References

1. Horn, A. & Fox, M. D. Opportunities of connectomic neuromodulation. *Neuroimage* **221**, 117180 (2020).
2. Siddiqi, S. H., Kording, K. P., Parvizi, J. & Fox, M. D. Causal mapping of human brain function. *Nat. Rev. Neurosci.* **23**, 361–375 (2022).
3. Hollunder, B. et al. Toward personalized medicine in connectomic deep brain stimulation. *Prog. Neurobiol.* **210**, 102211 (2022).
4. Grill, W. M., Snyder, A. N. & Miocinovic, S. Deep brain stimulation creates an informational lesion of the stimulated nucleus. *Neuroreport* **15**, 1137–1140 (2004).
5. Haber, S. N., Liu, H., Seidlitz, J. & Bullmore, E. Prefrontal connectomics: from anatomy to human imaging. *Neuropsychopharmacology* **47**, 20–40 (2021).
6. Haynes, W. I. A. & Haber, S. N. The organization of prefrontal-subthalamic inputs in primates provides an anatomical substrate for both functional specificity and integration: implications for basal ganglia models and deep brain stimulation. *J. Neurosci.* **33**, 4804–4814 (2013).
7. Haber, S. N. The primate basal ganglia: parallel and integrative networks. *J. Chem. Neuroanat.* **26**, 317–330 (2003).
8. Alexander, G., DeLong, M. R. & Strick, P. L. Parallel organization of functionally segregated circuits linking basal ganglia and cortex. *Annu. Rev. Neurosci.* **9**, 357–381 (1986).
9. Deffains, M. et al. Subthalamic, not striatal, activity correlates with basal ganglia downstream activity in normal and parkinsonian monkeys. *eLife* **5**, e16443 (2016).
10. Hardman, C. D. et al. Comparison of the basal ganglia in rats, marmosets, macaques, baboons, and humans: volume and neuronal number for the output, internal relay, and striatal modulating nuclei. *J. Comp. Neurol.* **445**, 238–255 (2002).
11. Deuschl, G. et al. A randomized trial of deep-brain stimulation for Parkinson's disease. *N. Engl. J. Med.* **355**, 896–908 (2006).
12. Ostrem, J. L. et al. Subthalamic nucleus deep brain stimulation in primary cervical dystonia. *Neurology* **76**, 870–878 (2011).
13. Lin, S. et al. Deep brain stimulation of the globus pallidus internus versus the subthalamic nucleus in isolated dystonia. *J. Neurosurg.* **132**, 721–732 (2019).
14. Mallet, L. et al. Subthalamic nucleus stimulation in severe obsessive-compulsive disorder. *N. Engl. J. Med.* **359**, 2121–2134 (2008).
15. Chabardes, S. et al. Deep brain stimulation of the subthalamic nucleus in obsessive-compulsives disorders: long-term follow-up of an open, prospective, observational cohort. *J. Neurol. Neurosurg. Psychiatry* **91**, 1349–1356 (2020).
16. Dai, L. et al. Subthalamic deep brain stimulation for refractory Gilles de la Tourette's syndrome: clinical outcome and functional connectivity. *J. Neurol.* **269**, 6116–6126 (2022).
17. Vissani, M. et al. Spatio-temporal structure of single neuron subthalamic activity identifies DBS target for anesthetized Tourette syndrome patients. *J. Neural Eng.* **16**, 066011 (2019).
18. Horn, A. et al. Optimal deep brain stimulation sites and networks for cervical vs. generalized dystonia. *Proc. Natl Acad. Sci. USA* **119**, e2114985119 (2022).
19. Irmen, F. et al. Left prefrontal connectivity links subthalamic stimulation with depressive symptoms. *Ann. Neurol.* **87**, 962–975 (2020).
20. Baldermann, J. C. et al. Connectomic deep brain stimulation for obsessive-compulsive disorder. *Biol. Psychiatry* **90**, 678–688 (2021).
21. Li, N. et al. A unified connectomic target for deep brain stimulation in obsessive-compulsive disorder. *Nat. Commun.* **11**, 3364 (2020).
22. Van Essen, D. C. et al. The WU-Minn Human Connectome Project: an overview. *Neuroimage* **80**, 62–79 (2013).
23. Wang, F. et al. In vivo human whole-brain Connectom diffusion MRI dataset at 760 μm isotropic resolution. *Sci. Data* **8**, 122 (2021).
24. Maier-Hein, K. H. et al. The challenge of mapping the human connectome based on diffusion tractography. *Nat. Commun.* **8**, 1349 (2017).
25. Noecker, A. M. et al. StimVision v2: examples and applications in subthalamic deep brain stimulation for Parkinson's disease. *Neuromodulation* **24**, 248–258 (2021).
26. Petersen, M. V. et al. Holographic reconstruction of axonal pathways in the human brain. *Neuron* **104**, 1056–1064 (2019).
27. Middlebrooks, E. H. et al. Neuroimaging advances in deep brain stimulation: review of indications, anatomy, and brain connectomics. *Am. J. Neuroradiol.* **41**, 1558–1568 (2020).
28. Ewert, S. et al. Toward defining deep brain stimulation targets in MNI space: a subcortical atlas based on multimodal MRI, histology and structural connectivity. *Neuroimage* **170**, 271–282 (2018).
29. Rodriguez-Oroz, M. C. et al. Initial clinical manifestations of Parkinson's disease: features and pathophysiological mechanisms. *Lancet Neurol.* **8**, 1128–1139 (2009).
30. Horn, A. et al. Teaching NeuroImages: in vivo visualization of Edinger comb and Wilson pencils. *Neurology* **92**, e1663–e1664 (2019).
31. Penfield, W. & Perot, P. The brain's record of auditory and visual experience: a final summary and discussion. *Brain* **86**, 595–696 (1963).
32. Albin, R. L., Young, A. B. & Penney, J. B. The functional anatomy of basal ganglia disorders. *Trends Neurosci.* **12**, 366–375 (1989).
33. DeLong, M. R. Primate models of movement disorders of basal ganglia origin. *Trends Neurosci.* **13**, 281–285 (1990).
34. Alexander, G. E. & Crutcher, M. D. Functional architecture of basal ganglia circuits: neural sustrates of parallel processing. *Trends Neurosci.* **13**, 266–271 (1990).
35. Percheron, G. & Filion, M. Parallel processing in the basal ganglia: up to a point. *Trends Neurosci.* **14**, 55–56 (1991).

36. Nambu, A., Tokuno, H. & Takada, M. Functional significance of the cortico-subthalamo-pallidal 'hyperdirect' pathway. *Neurosci. Res.* **43**, 111–117 (2002).

37. Corp, D. T. et al. Network localization of cervical dystonia based on causal brain lesions. *Brain* **142**, 1660–1674 (2019).

38. Inoue, K. et al. Disinhibition of the somatosensory cortex in cervical dystonia—decreased amplitudes of high-frequency oscillations. *Clin. Neurophysiol.* **115**, 1624–1630 (2004).

39. Prudente, C. N., Hess, E. J. & Jinnah, H. A. Dystonia as a network disorder: what is the role of the cerebellum? *Neuroscience* **260**, 23–35 (2014).

40. Neychev, V. K., Fan, X., Mitev, V. I., Hess, E. J. & Jinnah, H. A. The basal ganglia and cerebellum interact in the expression of dystonic movement. *Brain* **131**, 2499–2509 (2008).

41. Havrankova, P. et al. Repetitive TMS of the somatosensory cortex improves writer's cramp and enhances cortical activity. *Neuroendocrinol. Lett.* **31**, 73–86 (2010).

42. Bradnam, L. V., McDonnell, M. N. & Ridding, M. C. Cerebellar intermittent theta-burst stimulation and motor control training in individuals with cervical dystonia. *Brain Sci.* **6**, 56 (2016).

43. Desrochers, P., Brunfeldt, A., Sidiropoulos, C. & Kagerer, F. Sensorimotor control in dystonia. *Brain Sci.* **9**, 79 (2019).

44. Hassler, R., Riechert, T., Mundinger, F., Umbach, W. & Ganglberger, J. A. Physiological observations in stereotaxic operations in extrapyramidal motor dysturbances. *Brain* **83**, 337–350 (1960).

45. Horn, A. et al. Connectivity predicts deep brain stimulation outcome in Parkinson's disease. *Ann. Neurol.* **82**, 67–78 (2017).

46. Vanegas-Arroyave, N. et al. Tractography patterns of subthalamic nucleus deep brain stimulation. *Brain* **139**, 1200–1210 (2016).

47. Shirota, Y. et al. Supplementary motor area stimulation for Parkinson disease: a randomized controlled study. *Neurology* **80**, 1400–1405 (2013).

48. Nachev, P., Kennard, C. & Husain, M. Functional role of the supplementary and pre-supplementary motor areas. *Nat. Rev. Neurosci.* **9**, 856–869 (2008).

49. Li, N. et al. A unified functional network target for deep brain stimulation in obsessive-compulsive disorder. *Biol. Psychiatry* **90**, 701–713 (2021).

50. Carmi, L. et al. Efficacy and safety of deep transcranial magnetic stimulation for obsessive-compulsive disorder: A prospective multicenter randomized double-blind placebo-controlled trial. *Am. J. Psychiatry* **176**, 931–938 (2019).

51. Franzkowiak, S. et al. Motor-cortical interaction in Gilles de la Tourette syndrome. *PLoS ONE* **7**, e27850 (2012).

52. Worbe, Y. et al. Altered structural connectivity of cortico-striato-pallido-thalamic networks in Gilles de la Tourette syndrome. *Brain* **138**, 472–482 (2015).

53. Andrade, P. et al. Modulation of fibers to motor cortex during thalamic DBS in Tourette patients correlates with tic reduction. *Brain Sci.* **10**, 302 (2020).

54. Ganos, C. et al. A neural network for tics: insights from causal brain lesions and deep brain stimulation. *Brain* **145**, 4385–4397 (2022).

55. Johnson, K. A. et al. Structural connectivity predicts clinical outcomes of deep brain stimulation for Tourette syndrome. *Brain* **143**, 2607–2623 (2020).

56. Kleimaker, M. et al. Non-invasive brain stimulation for the treatment of Gilles de la Tourette syndrome. *Front. Neurol.* **11**, 592258 (2020).

57. Martino, D., Ganos, C. & Worbe, Y. Neuroimaging applications in Tourette's syndrome. *Int. Rev. Neurobiol.* **143**, 65–108 (2018).

58. Ashkan, K., Rogers, P., Bergman, H. & Ughratdar, I. Insights into the mechanisms of deep brain stimulation. *Nat. Rev. Neurol.* **13**, 548–554 (2017).

59. Neudorfer, C. et al. Kilohertz-frequency stimulation of the nervous system: a review of underlying mechanisms. *Brain Stimul.* **14**, 513–530 (2021).

60. Horn, A. et al. Lead-DBS v2: towards a comprehensive pipeline for deep brain stimulation imaging. *Neuroimage* **184**, 293–316 (2019).

61. Husch, A. et al. PaCER—a fully automated method for electrode trajectory and contact reconstruction in deep brain stimulation. *Neuroimage Clin.* **17**, 80–89 (2018).

62. Ewert, S. et al. Optimization and comparative evaluation of nonlinear deformation algorithms for atlas-based segmentation of DBS target nuclei. *Neuroimage* **184**, 586–598 (2019).

63. Vogel, D. et al. Anatomical brain structures normalization for deep brain stimulation in movement disorders. *Neuroimage Clin.* **27**, 102271 (2020).

64. Oxenford, S. et al. WarpDrive: improving spatial normalization using manual refinements. *Med. Image Anal.* **91**, 103041 (2024).

65. Baldermann, J. C. et al. Connectivity profile predictive of effective deep brain stimulation in obsessive-compulsive disorder. *Biol. Psychiatry* **85**, 735–743 (2019).

66. Amunts, K. et al. BigBrain: an ultrahigh-resolution 3D human brain model. *Science* **340**, 1472–1475 (2013).

67. Edlow, B. L. et al. 7 Tesla MRI of the ex vivo human brain at 100 micron resolution. *Sci. Data* **6**, 244 (2019).

68. Faria, A. V. et al. Atlas-based analysis of resting-state functional connectivity: evaluation for reproducibility and multi-modal anatomy-function correlation studies. *Neuroimage* **61**, 613–621 (2012).

69. Pauli, W. M., Nili, A. N. & Tyszka, J. M. A high-resolution probabilistic in vivo atlas of human subcortical brain nuclei. *Sci. Data* **5**, 180063 (2018).

[1]Movement Disorders and Neuromodulation Unit, Department of Neurology, Charité – Universitätsmedizin Berlin, Berlin, Germany. [2]Einstein Center for Neurosciences Berlin, Charité – Universitätsmedizin Berlin, Berlin, Germany. [3]Berlin School of Mind and Brain, Humboldt-Universität zu Berlin, Berlin, Germany. [4]Movement Disorders and Neuromodulation Centre, Department of Neurology, University of California, San Francisco, San Francisco, CA, USA. [5]Center for Brain Circuit Therapeutics, Department of Neurology, Brigham and Women's Hospital, Harvard Medical School, Boston, MA, USA. [6]Department of Neurosurgery, Massachusetts General Hospital, Harvard Medical School, Boston, MA, USA. [7]Department of Psychiatry and Psychotherapy, Charité – Universitätsmedizin Berlin, Berlin, Germany. [8]Université Grenoble Alpes, Grenoble, France. [9]Inserm, U1216, Grenoble Institut des Neurosciences, Grenoble, France. [10]Department of Psychiatry, Centre Hospitalier Universitaire Grenoble Alpes, Grenoble, France. [11]Unit of Functional Neurosurgery, UCL Queen Square Institute of Neurology, London, UK. [12]Victor Horsley Department of Neurosurgery, The National Hospital for Neurology and Neurosurgery, London, UK. [13]The BioRobotics Institute, Scuola Superiore Sant'Anna, Pisa, Italy. [14]Department of Excellence in Robotics and AI, Scuola Superiore Sant'Anna, Pisa, Italy. [15]Department of Neurosurgery, Rujin Hospital, Shanghai Jiao Tong University School of Medicine, Shanghai, China. [16]Department of Neurology, University Hospital Würzburg, Würzburg, Germany. [17]Department of Neurological Surgery, University of Pittsburgh, Pittsburgh, PA, USA. [18]Department of Psychiatry and Psychotherapy, Faculty of Medicine and University Hospital Cologne, University of Cologne, Cologne, Germany. [19]Department of Neurology, Faculty of Medicine and University Hospital Cologne, University of Cologne, Cologne, Germany. [20]Department of Stereotactic and Functional Neurosurgery, Faculty of Medicine and University Hospital Cologne, University of Cologne, Cologne, Germany. [21]Clinic of Pain and Functional Neurosurgery, São Paulo, Brazil. [22]Department of Neurology and Neurosurgery, University of Caxias do Sul, Rio Grande do Sul, Brazil. [23]Department of Neurology, Charité – Universitätsmedizin Berlin, Berlin, Germany. [24]NeuroCure Cluster of Excellence, Charité – Universitätsmedizin Berlin, Berlin, Germany. [25]Department of Psychiatry, Massachusetts General Hospital, Harvard Medical School, Boston, MA, USA. [26]Edmond and Lily Safra Center for Brain Sciences, The Hebrew University, Jerusalem, Israel. [27]Department of Medical Neurobiology, Institute of Medical Research Israel-Canada, The Hebrew University, Hadassah Medical School, Jerusalem, Israel. [28]Department of Neurosurgery, Hadassah Medical Center, Jerusalem, Israel. [29]Department of Neurology, Emory University School of Medicine, Atlanta, GA, USA. [30]Parkinson and Movement Disorders Unit, Fondazione IRCCS Istituto Neurologico Carlo Besta, Milan, Italy. [31]Department of Neuropsychiatry, The National Hospital for Neurology and Neurosurgery, London, UK. [32]Department of Neurosurgery, Centre Hospitalier Universitaire Grenoble Alpes, Grenoble, France. [33]Department of Neurological Surgery, University of California, San Francisco, San Francisco, CA, USA. [34]These authors contributed equally: Ningfei Li, Andreas Horn. ✉e-mail: ningfei.li@gmail.com; ahorn1@bwh.harvard.edu

Methods

Patient cohorts, imaging and clinical assessments

Every stage of the research process complied with all relevant ethical regulations, and post hoc analyses performed for the purpose of the present manuscript were approved by the institutional review board of Charité – Universitätsmedizin Berlin (master vote EA2/186/18). Procedures of clinical trials and studies leading to the collection of these data were approved by the institutional review boards at each of the respective data collection sites. They were carried out in accordance with the 1975 Declaration of Helsinki, and all participants signed an informed consent before study participation. Participants received no compensation in exchange for taking part in this research.

Discovery cohort. The present study sought to establish models of optimal focal stimulation sites and streamlines, harnessing a retrospective discovery sample of eight patient cohorts ($n = 197$) spanning seven international DBS centers (San Francisco, Shanghai, Berlin, Würzburg, Grenoble, London and Pisa/Milan). Each of these patients had been bilaterally implanted with subthalamic DBS for treatment of DYT ($n = 70$), PD ($n = 94$), TS ($n = 14$) or OCD ($n = 19$). The full sample consisted of two patient cohorts per disease, with the Shanghai center contributing two cohorts (DYT and TS data). Among all available patients with complete neuroimaging and clinical outcome information, no patient was discarded from our analyses. Instead of prospective randomization, we leveraged incidental variability in electrode placement within each disease cohort, which can be presumed to be random. Supplementary Table 1 summarizes the included discovery cohorts, with more detailed patient-wise demographic and clinical information listed in Supplementary Tables 2–5.

Given the exploratory nature of our study, no statistical methods were used to pre-determine sample sizes. As neuropsychiatric applications of STN-DBS are recent and rare, samples, especially in TS and OCD, are limited by the small number of worldwide surgeries. In the TS cohort, we included all globally treated patients undergoing STN stimulation for this condition at the time of analysis. Overall, we were able to include two cohorts per disease group. Our initial assumption of expected effect sizes was based on Li et al.[21] and Treu et al.[70], with an R of approximately 0.4 for reported correlations between empirical clinical outcomes and estimated gain scores. In view of the natural restrictions in available sample sizes, we calculated a 'compromise' type power analysis using G*Power, version 3.1.9.6 (refs. [71,72]), to determine the power of our analyses based on the accessible data per disorder to detect the assumed effect. Given a β/α ratio of 1, the available DYT sample ($n = 56$ in the main cohort) used for the model setup was powered to 0.94, the PD sample ($n = 94$) to 0.98, the TS sample ($n = 14$) to 0.77 and the OCD sample ($n = 19$) to 0.81 for detecting the assumed effect size. To our knowledge, this is the largest transdiagnostic study of its kind.

Retrospective validation cohorts. To further validate streamline models in two exemplary disorders based on out-of-sample data, two additional patient cohorts were integrated. The first consisted of a further cohort of patients with PD from Würzburg receiving STN-DBS ($n = 32$). The second comprised an additional cohort of patients with OCD, pooled across London, Cologne and Boston centers, treated with DBS of the VC/VS region ($n = 35$). Crucially, these patients contributed entirely independent data points that had not been used to inform the previous streamline model setup. The only exception was formed by the OCD-DBS cohort from London, in which patients had received a set of electrodes each to both targets (STN and VC/VS, with $n = 4$ electrodes per patient) that had been activated independently during the original study[73]. For this cohort, stimulation settings and clinical scores with 'optimized' stimulation of both targets combined or of each target separately were available. For model generation within the discovery cohort (with subthalamic focus), stimulation parameters and corresponding Y-BOCS improvement values collected during the 'STN-DBS-only' phase

were implemented, whereas corresponding information acquired during the 'VC/VS-DBS-only' phase was used to inform the retrospective OCD model validation. Supplementary Table 6 summarizes these two additional retrospective cohorts. Patient-specific information is provided in Supplementary Table 7 (PD validation cohort) and Supplementary Table 8 (OCD validation cohorts). Again, none of the available patients with complete neuroimaging and clinical information was excluded from further analysis.

Prospective patient cases. Streamline models for PD and OCD were further prospectively validated by reprogramming DBS settings in a patient with PD and in a patient with OCD from Würzburg and Boston, respectively, guided by the aim of maximized engagement of their stimulation volumes with the corresponding streamline model. Both patients were recruited and investigated within the ongoing clinical service—namely, in the inpatient DBS program at University Hospital Würzburg in the case of the patient with PD or in the DBS program of the psychiatry and neurosurgery departments at Massachusetts General Hospital (MGH) in the case of the patient with OCD.

Finally, a single patient with OCD from São Paulo underwent DBS surgery and programming as informed by the OCD streamline model. This patient was recruited within the regular surgical service of Clínica de Dor e Funcional after classification as a refractory case of OCD that was associated with depression. He underwent evaluation by a neurologist, a psychologist and two functional neurosurgeons before approval of the DBS implantation surgery by the Ethics Board Committee of the State of Rio Grande do Sul. Supplementary Table 11 provides additional details on these three patient cases.

To inform surgical planning and for exclusion of structural abnormalities, all patients received high-resolution multi-spectral structural MRI that had been acquired at 3T field strength. High imaging quality was ensured through visual inspection by a multi-disciplinary team during stereotactic planning, and, in case of movement artifacts, pre-operative acquisitions were repeated under general anesthesia. Intra-operative microelectrode recordings and macrostimulations as well as either post-operative MRI ($n = 73$) or computed tomography (CT) of the head ($n = 188$) (Supplementary Tables 1–8 and 11) were acquired to confirm accurate lead placement.

Specifics on electrode models implanted in each cohort used for the model setup are summarized in Supplementary Table 1, and the same information for retrospective model validation cohorts and prospective patient cases is provided in Supplementary Tables 6 and 11, respectively. Stimulation settings and corresponding clinical improvement scores for all cohorts were selected from times of follow-up to which stimulation effects had sufficiently stabilized (Supplementary Tables 1, 6 and 11).

Times of follow-up available for some patients within the $n = 58$ cohort of patients with DYT from Shanghai were shorter than those of other disease cohorts. In addition, as DYT is a heterogeneous disease of several forms (for example, generalized, segmental and focal somatotopic expressions), pre-operative BFMDRS summary scores in some Shanghai patients were considerably lower than those of patients in the San Francisco cohort. To ascertain stabilized and comparable DBS effects across cohorts, main analyses were, thus, carried out on the DYT sample including a subcohort of Shanghai patients ($n = 44$), which sufficed to more conservative inclusion criteria (baseline BFMDRS scores ≥5 and follow-up ≥6 months). However, we repeated our results on the complete DYT sample ($n = 70$) including the full Shanghai cohort ($n = 58$) to demonstrate stability of effects (Supplementary Fig. 10).

Clinical outcome data and DBS parameters were retrieved from the collecting sites using Microsoft Excel, version 16.70, and imported for analysis using MATLAB R2022b, version 9.13.0.2105380 (MathWorks). Clinical improvement was measured in the form of relative change from pre-operative baseline to post-operative follow-up under DBS ON (or from post-operative OFF to ON DBS conditions in the case of PD) within the primary outcome assessment of each disease cohort: BFMDRS in

DYT, UPDRS-III in PD, Y-BOCS in OCD and YGTSS in TS. Blinding was not relevant in the case of the secondary analyses of existing datasets performed here. To mitigate the risk of observer bias, we tested the explanatory value of our models in hold-out data and performed retrospective and prospective validation experiments (see below).

Of note, most statistical results in the present manuscript involve Spearman's rank correlations, which do not make assumptions about the underlying distribution. In addition, for these results, scatter plots of individual data points are shown. For analyses in which t-tests were calculated, normality and equality of variances were formally tested (and present for all cases).

DBS electrode localization and E-field modeling

DBS electrodes of all patients were localized based on default settings in an advanced, state-of-the-art processing pipeline as implemented in Lead-DBS software, version 3.0 (https://www.lead-dbs.org)[74]. MATLAB R2022b, version 9.13.0.2105380, was used to apply this Lead-DBS-based analysis stream. In brief, our approach involved linear co-registrations of post-operative head CT or MRI scans to pre-operative T1-weighted images by means of Advanced Normalization Tools (ANTs; http://stnava.github.io/ANTs/)[75]. Co-registration results were subsequently corrected for potential intra-operative brain shift via an automated subcortical refinement module (as implemented in Lead-DBS) but also needed to conform to meticulous visual inspection by two expert users (B.H. and N.L.). This latter step led to manual refinement in cases where aberrations were detected.

All pre-operative acquisitions were used for multi-spectral spatial normalization into ICBM 2009b Nonlinear Asymmetric ('MNI') template space[76] using the Symmetric Normalization (SyN) approach included in ANTs with the 'effective: low variance + subcortical refinement' preset in Lead-DBS. This method had outperformed similar approaches for subcortical normalizations (including STN segmentation) across >10,000 nonlinear warps and different normalization techniques in two independent studies, with precision approaching manual expert segmentation[62,63]. For all analyses and visualizations of results, atlas definitions of the STN were based on the DBS Intrinsic Template (DISTAL) atlas, version 1.1 (ref. 28), a precise subcortical atlas explicitly created for use within Lead-DBS and based on convergent information from multi-modal MRI, histology and structural connectivity.

To maximize registration accuracy further, normalization warp fields were manually refined using the WarpDrive[64] toolbox included in Lead-DBS, version 3.0 (ref. 74), wherever mismatches in the registration were clearly visible and with particular attention to the STN as the anatomical structure in focus. Although high registration precision between a template brain and individual brain anatomy is of utmost importance for accurate reconstructions of electrode localizations, the low contrast of basal ganglia structures on typically applied clinical imaging sequences renders the automated registration between an individual and an atlas STN challenging[62,77]. WarpDrive is conceived as a dedicated but optional module that allows to manually counteract small misalignments after automated normalization has been performed. Supplementary Fig. 11 shows examples of optimized normalization warp fields after manual WarpDrive refinements (ANTs + WarpDrive) in head-to-head comparison to unrefined, direct results of the automated pipeline (ANTs only). Across the entire discovery cohort, displacements of 0–1 mm were applied in $n = 296$ electrodes, of 1–2 mm in $n = 82$ electrodes and of >2 mm in $n = 16$ electrodes.

Subsequently, electrodes were pre-localized using the phantom-validated Precise and Convenient Electrode Reconstruction for Deep Brain Stimulation (PaCER) algorithm[61] in the case of post-operative CT. In the case of post-operative MRI, the trajectory search/contact reconstructions (TRAC/CORE) algorithm[78] was implemented instead, both as included in Lead-DBS, version 3.0 (ref. 74). The resulting pre-localizations were visually inspected and manually refined by two experienced users (B.H. and N.L.).

Integrating patient-specific active electrode contacts with corresponding stimulation parameters, the E-field as the gradient distribution of electrical potential in space was simulated in native patient space via an adaptation of the SimBio/FieldTrip pipeline (https://www.mrt.uni-jena.de/simbio/ and http://fieldtriptoolbox.org/)[79] as implemented in Lead-DBS, version 3.0 (ref. 74). Using a finite element (FEM) approach, a volume conductor model was created on the basis of a four-compartment mesh[60], which involves a realistic three-dimensional model of electrodes (metal and insulating electrode aspects) and surrounding anatomy (gray and white matter). Again, gray matter was defined using the DISTAL atlas, version 1.1 (ref. 28). Finally, electrodes and E-fields were transformed into template space based on the (manually optimized) warp fields priorly determined during normalization of pre-operative MRI acquisitions. These steps allowed for visualization and analysis of electrodes and stimulation fields at the group level using the Lead-Group toolbox[70] as well as DBS Sweet Spot and Fiber Filtering Explorers[74].

Dysfunction mappings at the subthalamic level

Model definition (Fig. 1a). Our group-level approach intended to delineate and compare the organization of disorder-specific stimulation effects across different neuroanatomical levels, namely (1) that of the subthalamic target site (DBS Sweet Spot Mapping) as well as (2) that of fronto-subthalamic pathways and interconnected cortical sites (DBS Fiber Filtering).

In the first part of our analysis stream, DBS Sweet Spot Mapping[18] (Fig. 1a) was performed in each disease cohort separately to identify subthalamic voxels linked to optimal stimulation-related improvements within each respective cardinal dysfunction. For this purpose, information from patient-specific E-fields was integrated with corresponding clinical outcome scores. The E-field denotes the first derivative of the estimated voltage distribution administered to voxels in space, exhibiting greater intensity near active electrode contacts and diminishing rapidly as distance increases. On a voxel-by-voxel basis, the E-field magnitude in each voxel encompassed by the E-field volume was denoted for each patient across the cohort. To account for variability in voxels covered across E-fields within each cohort and to circumvent unrepresentative results biased by too few data points, the region of interest (ROI) was limited to brain voxels encompassed by at least 50% of E-fields exceeding a magnitude threshold of 200 V/m. This E-field magnitude corresponds to a commonly assumed estimate of voltage needed to activate axons[45,80,81] and has been repeatedly successfully applied in models of DBS effects on anatomy surrounding the active electrode contact across disorders (for example, in refs. 19,82). Nonetheless, sweet spot modeling and corresponding quantitative validations were repeated for a range of different thresholds (that is, 180 V/m, 200 V/m and 220 V/m) to demonstrate robustness of results (Supplementary Fig. 1). For each considered voxel, this procedure resulted in a vector of E-field magnitude values of the length of the respective patient sample.

Iterating through brain voxels encompassed by the group of thresholded E-fields in template space, Spearman's rank correlations were calculated between the vector of E-field magnitudes and the vector of relative clinical improvements of all patients. This procedure resulted in a map of positive peak voxels associated with beneficial stimulation effects (sweet spot) as well as negative peak voxels related to detrimental stimulation effects (sour spot). The resulting model can be conceived as an optimal map of where E-fields should ideally stimulate the focal anatomy to maximize treatment success within the respective domain of dysfunction. Of note, these correlation coefficients should not be interpreted as significant results due to the mass-univariate (voxel-wise) nature of our analysis. Instead, they were validated by probing model performance in estimating clinical outcomes in a five-fold CV design (see below).

Estimation of outcomes based on the model. Once optimal sweet spot models had been established in each disease cohort, each model was tested for its explanatory value for clinical outcome variance. To do so, magnitudes of individual E-fields were multiplied with the model in a voxel-wise fashion, and results were averaged across voxels. This led to the attribution of one 'Sweet Spot Score' per E-field, and scores were finally averaged across bilateral E-fields to achieve one single Sweet Spot Score per patient. Our modeling approach followed the logic that E-fields in which peaks spatially overlapped highly with the sweet spot (receiving a high positive Sweet Spot Score) would be associated with considerable clinical improvements, whereas E-field peaks markedly encompassing the sour spot (high negative Sweet Spot Score) would result in low or negative estimates. To probe the tenability of this hypothesis, we performed in-sample Spearman's correlations (two-sided tests) between Sweet Spot Scores and empirical clinical outcomes across the cohort. More precisely, the model was calculated on the full discovery cohort, and E-field overlap with it was used to estimate clinical outcomes in each discovery patient. Although representing circular outcomes, these in-sample correlations allowed to compare results (1) across disorders and (2) between sweet spot and sweet streamline findings.

To investigate the generalizability of these results, we further tested whether disease-wise models were robust when subjected to a fivefold CV design, where the sweet spot model was built on a subset of four-fifths of the respective disorder's discovery cohort (training set) in each of the five folds, and results were used to estimate clinical outcome of the remaining (held-out) fifth of patients (test set). Crucially, because data of remaining patients were not used to inform the model, respectively, the CV strategy was unbiased by circularity. Once estimates for all patients had been derived, the sweet spot model accuracy was finally tested by correlating model-based Sweet Spot Scores with empirical outcomes across the disease cohort. In all analyses, *P* values were derived based on permuted testing building on 5,000 iterations.

Visualization of subthalamic dysfunction mappings. Disease-wise sweet spots were smoothed by a kernel of two at full width at half maximum using Statistical Parametric Mapping (SPM12) software (https://www.fil.ion.ucl.ac.uk/spm/) to visualize the organizational pattern of subthalamic dysfunction mappings across disorders. Smoothed profiles were projected onto the surface of a three-dimensional model of the STN in ICBM 2009b Nonlinear Asymmetric space derived from the DISTAL atlas, version 1.1 (ref. 28), using Surf Ice software, version 1.0.20211006 (https://www.nitrc.org/projects/surface). Three-dimensional density plot renderings of sweet spots were further generated by plotting R value magnitudes coded by spheres with different sizes and alpha values in space using Lead-DBS, version 3.0 (ref. 74). Namely, the size and alpha value (transparency) of spheres were weighted by the correlation of modulating the coordinate with clinical outcomes, so that higher correlation results were visualized in the form of larger and less transparent spheres. Two-dimensional axial and coronal views of sweet and sour spots were additionally displayed separately for each disorder using 3D Slicer software, version 5.2.1 (https://www.slicer.org/).

Dysfunction mappings at streamline and cortical levels
Model definition (Fig. 1b). The second part of our analysis stream followed the intention of deriving the topographical organization of dysfunction mappings (1) at the level of hyperdirect fronto-subthalamic streamlines and (2) that of interconnected sites within the frontal cortex.

To understand the relationship between DBS-based modulation of specific streamlines and a given clinical effect, we, thus, harnessed a previously validated structural connectivity analysis, termed DBS Fiber Filtering[65] (Fig. 1b), in an adapted form for implementation in (non-binarized) E-fields[19]. Structural connectivity was primarily defined by a population-based group connectome derived from multi-shell

dMRI-based tractography data of 985 healthy participants acquired within the HCP 1,200 subjects release[22]. Details on the calculation procedure of this connectome are reported in Li et al.[21]. In brief, computation of a whole-brain connectome for each of the 985 healthy patients was performed using the Lead-Connectome tool, as provided within the Lead-DBS environment, version 2.0 (ref. 60) (https://www.lead-dbs.org/about/lead-connectome/). Normalization of streamlines into template space involved a multi-spectral warp building on T1-weighted, T2-weighted and diffusion-weighted acquisitions through use of ANTs (using the 'Effective Low Variance' preset in Lead-DBS, version 2.0 (ref. 60)). In total, 6,000 streamlines were sampled per individual, which were finally aggregated across all 985 HCP participants to form a collective dataset in MNI space (encompassing a total of 6,000,000 fibers).

Although, by design, normative connectivity is unable to fully account for patient-specific anatomical variability, it is optimally suited for 'broad lens' insight into the average human brain at particularly high resolution, as precisely aimed at in the present investigation. Although small inter-individual differences in the topography of human fronto-subcortical interconnections exist, at least a general agreement can be presumed (Supplementary Fig. 12). To assess the general topography of cortico-subthalamic interconnections, we seeded streamlines from five seed points that were manually placed along the dorsal convex shape of the STN in standard space (Supplementary Fig. 12a). We normalized streamlines originating from nine random individual HCP subjects and selected streamlines that connected to each of the seed points in individualized connectomes (Supplementary Fig. 12b). This enabled visual comparability between the topography of STN connections. Although, as expected, the general fronto-rostral topography of interconnections between cortex and STN was revealed in all nine individuals (Supplementary Fig. 12c), the results also show individual variance. In this context, we must mention that only an unknown fraction of these differences should be attributed to true anatomical variance. As demonstrated by several authors using test–retest analysis of brains that were scanned multiple times with dMRI, a substantial fraction of individual differences needs to be attributed to noise and distortions in the data, the choice of MRI machine and tractography algorithms[83,84].

Again, the streamline modeling procedure was performed in each disease cohort separately. Per disorder-wise cohort, we first isolated the subset of streamlines from the normative connectome that passed in proximity of at least a minimal number of electrodes. These were characterized in the form of streamlines traversing a rather high E-field magnitude (>0.8 V/mm) close to active contacts in more than 0.5% of E-fields within that cohort. Iterating through this subset of streamlines, one streamline at a time, the stimulation impact per E-field on each streamline was estimated by the peak value among E-field magnitudes collected from points along its passage. This resulted in a 'streamlines by E-field peaks' matrix in which each entry denoted the peak impact of each E-field on each streamline.

Second, the entries of the 'streamlines by E-field peaks' matrix were Spearman's rank correlated with clinical improvements across the disease cohort. Following this procedure, each streamline was tagged by an R value coding for the association strength of its modulation with clinical outcome. The resulting streamline profile can be seen as a model of optimal connectivity for maximal clinical improvements, where streamlines with positive weights would be strongly modulated by E-fields of good performers (sweet streamlines) and such with negative weights by E-fields of poor performers (sour streamlines). As these correlation coefficients relied on a mass-univariate approach, streamline profiles were later validated by probing their capability to estimate clinical improvement in data that had not been used to inform the model (see below).

Estimation of outcomes based on the model. To determine how well disease-wise optimal sweet streamline profiles would perform in

estimating clinical improvement in single patients, the peaks of their E-fields were overlapped with the streamline model of optimal electrode connectivity. Specifically, streamlines from the model touched by that E-field were first isolated. Iterating through this subset, the R value of each streamline was subsequently multiplied by the peak E-field magnitude to account for the strength of its modulation by this E-field. Moreover, only the peak 5% of these weighted sweet streamline R values were retained to maximally account for the streamlines most impacted on by that E-field. These top 5% of weighted R values were then summed up, so that each E-field was tagged by the 'weighted peak 5% of Fiber R scores'. Because each patient within the cohorts considered in the present study had been implanted to the STN at both hemispheres, the Fiber R score was finally averaged across bilateral E-fields to result in one single value per patient.

Following the logic of this procedure, E-field peaks displaying high overlaps with beneficial streamlines would receive high clinical scores, whereas those with no (or merely peripheral) overlap would receive low clinical estimates. A subset of the most relevant sweet streamlines was selected for this validation step using an R value threshold set at the top 1% of the cumulative distribution function of R values of all streamlines. This pre-selection step included such streamlines where high modulation had led to high improvement (with high meaningfulness for the model) while discarding potentially less relevant or noisy correlations.

Model validation within the discovery cohort followed a similar strategy as implemented in the case of Sweet Spot Mapping. Specifically, we tested for an association between spatial overlap of a patient's E-fields with the model (weighted peak 5% of Fiber R scores) with empirical clinical improvements across patients using Spearman's correlation (two-sided test). In doing so, the ability of streamline models to explain in-sample variance could be scrutinized for comparability of results (1) across disorders and (2) with sweet spots. For in-sample analyses, sweet streamline models were derived based on E-fields of all patients within each disease cohort and validated using each patient of the respective sample (circular analysis). Ultimately, all models were subjected to CVs in a fivefold design to investigate the generalizability of their explanatory value in hold-out data. Again, this approach was implemented by randomly splitting each disorder's discovery patient cohort into five folds. The disease-specific model was built on four-fifths of patients and validated on the remaining fifth. This strategy was repeated five times, so that model-based estimates (weighted peak 5% of Fiber R scores) were obtained for all patients across all folds. These estimates could then be correlated with empirical clinical outcomes to evaluate model validity in a non-circular fashion. Again, P values were calculated using permutation testing based on 5,000 iterations.

Visualization of cortical dysfunction mappings. To elucidate the topographical organization of interconnected fronto-cortical regions, disease-wise sets of sweet streamlines were first converted to voxelized images (streamline density maps). The resulting maps were then smoothed using an 8-mm Gaussian kernel at full width at half maximum as implemented in SPM12 (https://www.fil.ion.ucl.ac.uk/spm/) and projected onto the cortical surface of the MNI template using Surf Ice software, version 1.0.20211006 (https://www.nitrc.org/projects/surfice). Anatomical correlates of disease-wise cortical sites interconnected with sweet streamlines were then defined based on the Johns Hopkins University (JHU) atlas parcellation[68].

Quantification of spatial uncertainty. Furthermore, we aimed to quantify and visualize the degree of spatial uncertainty per streamline within disorder-wise dysfunction mappings at the streamline level. For this purpose, the thickness of each streamline was determined by the $-\log(P)$ value, meaning that thicker streamlines would be illustrative of lower P values.

Influence of electrode placement. Subsequently, we intended to scrutinize the relative impact of different model inputs. Besides the choice of a normative connectome, DBS Fiber Filtering results are determined mainly by two major sources of variability across patients—namely, (1) by the precise placement of the stimulation volume and (2) by clinical improvements. In three out of the four disorders of interest in the present study (DYT, PD and TS), stereotactic targeting aims at the same site within the dorsolateral aspect of the STN, whereas the OCD target resides more antero-medially. Thus, the partitioning of dysfunction mappings among various disorders could predominantly be driven by the stimulation impact on clinical outcomes and may not rely solely on differential electrode placement.

To investigate this hypothesis, we implemented a total of three data-driven control analyses. First, plain streamline connections seeding from bilateral stimulation volumes were isolated for each disorder. These comprised the entirety of structural connections activated by a bilateral E-field, irrespective of the importance of their modulation for clinical outcome. Among these, only the subset of streamlines shared across disorders was retained and contrasted to disease-specific sweet streamlines. Four-sample and pairwise tests for equality of proportions (two-sided tests) were performed to compare the degree of overlap between them.

Second, we fit a three-dimensional Gaussian distribution to the standard (second-to-lowest) electrode contacts of all patients with a specific disorder, leading to four blurred volumes within the STN. Streamlines were then seeded from each of these Gaussians as ROIs. The partitioning among the resulting disease-wise connectivity profiles was consequently visually compared to the streamline segregation model that had been achieved using DBS Fiber Filtering. In the latter approach, streamlines connected to empirical stimulation volumes of patients had been weighted by stimulation-related outcomes within the four different domains of dysfunction.

Third, each connection within each respective sweet streamline model per disorder was color-coded by a specificity value, which was calculated by dividing its R value by the average of R values that it received across the three remaining disorders. The streamline segregation result of this approach was finally visually compared to that of the connectivity profile that had been established based on 'conventional' color-coding as informed by a streamline's unbiased R value (resulting from our DBS Fiber Filtering analysis).

Model specificity. Besides validation of each model within the respective disorder that it had been calculated on, we were interested in the degree of specificity of disease-wise models in their ability of explaining clinical outcome variance. To demonstrate specificity, we considered the sweet streamline models for each disorder and overlapped E-fields of patients in all remaining three disorders with the model to predict clinical outcomes in a disorder-by-disorder fashion. Details of this cross-prediction approach were equivalent to those of the CV strategy described above. In brief, weighted peak 5% of Fiber R scores were estimated for each patient based on the degree to which their E-fields encompassed the model, and, finally, Spearman's correlations were performed between these estimates and the empirical clinical outcomes across the cohort of patients to test for model accuracy. In the case of specificity of dysfunction mappings, each of the models would show predictive utility uniquely for clinical improvements within the corresponding outcome measure (good fit between estimates and outcomes) but not for those of other clinical scales (poor fit).

Influence of choice of connectome. Furthermore, we aimed to scrutinize the influence imposed by a particular normative resource chosen to inform connectivity in our DBS Fiber Filtering analyses. To do so, we repeated modeling and model validation procedures using five additional connectomes based on otherwise equivalent model parameters.

The first such resource consisted of a normative whole-brain connectome, derived from a multi-shell diffusion-weighted imaging dataset at 760-µm isotropic diffusion acquired in vivo in a single healthy participant over a total duration of 18 scanning hours[23] (MGH Single Subject 760 µm Connectome; openly available from https://datadryad.org/stash/dataset/doi:10.5061/dryad.nzs7h44q2). Although generalizability of results derived using this connectome to a larger population is naturally limited by its single-patient origin, it lends itself particularly well for detailed anatomical insight and visualization by dint of its unprecedented imaging resolution.

Second, an axonal pathway atlas[26] (Basal Ganglia Pathway Atlas; openly available from https://osf.io/mhd4z/) was implemented, which did not rely on tracking of streamlines based on dMRI data and, thus, circumvents some of the most important drawbacks of dMRI-based tractography (such as the possibility of integrating false-positive connections)[24]. Instead, streamlines included in this tractogram were manually defined by expert anatomists within an advanced augmented reality (holography) framework. Guided by control points, this technique allows for precise localization and reconstruction of basal ganglia anatomy aided by three-dimensional images created from laser beams. Although the expert-characterized nature of this resource ensures a highly accurate representation of empirically existing (true-positive) connections, it is limited by a higher degree of false-negative streamlines (as the focus in its creation by the expert anatomists lies in accuracy at the expense of exhaustiveness).

Third, we employed a custom-made pathway atlas (DBS Tractography Atlas, version 2.1; openly available from https://github.com/netstim/DBS-Tractography-Atlas.git) informed on previously defined pathway atlases, including the DBS Tractography Atlas, version 1 (ref. 27), and the aforementioned Basal Ganglia Pathway Atlas[26]. It was completed by additional streamline tracking with focus on a comprehensive description of subthalamic interconnections with multiple cortical and subcortical nodes, leading to a finite set of 6,525,876 streamlines. Its creation specifically followed the intention of representing streamlines that had previously lacked delineation in other resources.

To generate this atlas, a first subset of streamlines connecting the STN to different cortical regions was derived via streamline tracking based on the HCP-1,065 diffusion data, which scanned 1,065 young and healthy adults[85]. These data are openly available within DSI-Studio (https://brain.labsolver.org/hcp_template.html; fiber orientation maps at 1-mm resolution). Using DSI-Studio (https://dsi-studio.labsolver.org/), the STN as defined within the DISTAL atlas, version 1.1 (ref. 28), was specified as an end region, and 1,500 streamlines were tracked from each of nine cortical Brodmann areas (BAs) as ROIs from the digitized Brodmann atlas[86]. These comprised BA1/2/3 (primary and secondary somatosensory cortex), BA4 (primary motor cortex), BA6 (supplementary motor area), BA10 (fronto-parietal cortex), BA13 (insular cortex), BA24/32 (cingulate cortex), BA25 (subgenual anterior cingulate cortex) and BA45/47 (frontal gyrus). Two further ROIs of the subcortical region—the substantia nigra pars compacta and pars reticulata—were added from the California Institute of Technology reinforcement learning atlas, version 1.1 (CIT168)[69].

To enable cortical branching, the angular threshold was set to a range of 60°–90°. Sampling was thresholded at a minimum length of 5 mm to avoid the inclusion of short streamlines and to prioritize long-range cortico-subthalamic projections. Streamline tracking between STN and substantia nigra aspects was performed based on a minimal tracking length of 10 mm, considering the distance between these two regions. To account for the exploratory nature of these connections, 20 iterations of topology-informed pruning were further implemented to limit the possibility of including false-positive streamlines[87]. Because of the role of these cortical regions in neuromodulation for affective disorders[88], streamline tracking between BA24/25/32 was seeded from the limbic aspect of the STN (based on its definition within the DISTAL atlas, version 1.1 (ref. 28)). In this case, a twofold dilation of

the limbic STN was implemented to allow for limbic regions adjacent to the anterior STN to be included[6], and streamlines were mirrored between hemispheres (thus increasing the streamline count per sampling to a total of 3,000) to limit the occurrence of potential spurious lateralization effects.

In addition, the creation of this anatomically inclusive pathway atlas was complemented by representations of the anterior thalamic radiation, the cerebellothalamic tract, the dentato-rubro-thalamic tract and the fasciculus subthalamicus from the DBS Tractography Atlas, version 1 (ref. 27). Finally, definitions of the ansa and fasciculus lenticularis as well as subthalamic-pallidal connections between STN and all pallidal nuclei were added from the Basal Ganglia Pathway Atlas[26], comprising interconnections between STN and internal pallidum (GPi), STN and GPe, Gpi and STN (associative and somatomotor aspects) and Gpe and STN (associative and somatomotor aspects).

Last, we aimed to demonstrate the validity of our findings in the face of disease-specific connectivity alterations in consequence of two exemplary brain circuit disorders. To this end, we repeated our DBS Fiber Filtering approach in a group connectome informed on diffusion scans acquired before surgery in the $n = 6$ patients with OCD (one female, mean age = 45.50 ± 10.52 years) from London. The supplementary materials of the original publication[73] contain more detailed information on scanning parameters. In brief, transformations from patient space into ICBM 2009b NLIN asymmetric space were derived using ANTs (http://stnava.github.io/ANTs/)[75]. dMRI data were pre-processed using FMRIB Software Library (FSL)[89], release 6.0 (https://fsl.fmrib.ox.ac.uk/fsl/fslwiki/FSL) (topup and eddy). A generalized q-sampling approach[90] was performed as implemented in DSI-Studio (http://dsi-studio.labsolver.org/). In total, 500,000 streamlines were deterministically tracked per patient with an angular threshold of 30 and a smoothing factor of 1, and default settings were kept for all remaining parameters.

A second disease-matched group connectome[28] was finally implemented that had previously been calculated based on data by $n = 85$ patients with PD (28 females; mean age = 59.48 ± 10.39 years) from the Parkinson's Progressive Marker Initiative[91] (PPMI; https://www.ppmi-info.org/). This connectome (PPMI-85, version 1.1; openly available from https://www.lead-dbs.org/helpsupport/knowledge-base/atlasesresources/normative-connectomes/) has been repeatedly used in the DBS context (for example, in refs. 19,45). Details on scanning parameters can be derived from the project website (https://www.ppmi-info.org/), and specifics on the creation of the resulting PD group connectome[28] are reported elsewhere[28]. In brief, a fast diffeomorphic image registration algorithm[92] (Diffeomorphic Anatomical Registration Through Exponentiated Lie Algebra (DARTEL)), as implemented in SPM12 (http://www.fil.ion.ucl.ac.uk/spm/software/spm12/) and Lead-DBS, version 2.0 (ref. 60), was applied per subject, to estimate a nonlinear deformation field into ICBM 2009b NLIN asymmetric space based on T2-weighted acquisitions. To determine global streamline sets, a generalized q-sampling approach[90] was run as available in DSI-Studio (http://dsi-studio.labsolver.org/). Specifically, 20,000 streamlines were sampled for each patient, using seeds within a white matter mask derived from segmenting the T2-weighted acquisitions using SPM12. Subsequently, the streamline set per patient was standardized into MNI space, employing the methodology described in refs. 93,94.

Of note, the terms 'fibers' or 'tracts' should ideally be reserved for anatomical images and not be used to refer to derivatives of tracking algorithms delineating pathways based on water molecule diffusion within the brain. Instead, dMRI-based tractography is an indirect estimate of physical connections—or axons—and cannot inform on their directionality within the brain[5]. Thus, we speak of 'streamlines' to refer to tracking results throughout the manuscript. For reasons of consistency with previous publications, we solely maintain the term 'DBS Fiber Filtering' here to denote our streamline modeling approach.

Retrospective and prospective streamline model validations

Retrospective model validations. Models informed on data points from the discovery cohort were further externally validated based on fully independent data (see above for the exception of the patients with OCD from London). In the two retrospective validation analyses, this strategy was carried out using the exact same approach as the CV analyses performed within the discovery sample—that is, by calculating the peak magnitude of each E-field at the intersection with each streamline of the respectively corresponding model (PD/OCD) and correlating the resulting aggregated value (weighted peak 5% of Fiber R score) with empirical clinical improvements.

Prospective model validations. In both patient cases receiving model-guided stimulation parameter optimization, reprogramming for clinical purposes took place based on a multi-disciplinary assessment of DBS location and streamline information. In the first reprogramming case of a patient with PD from Würzburg implanted to the STN, UPDRS-III scores were taken under DBS and dopaminergic medication OFF (after a 12-h-long washout period), under active DBS (medication OFF) with clinical DBS settings as well as under settings that maximized overlap of stimulation volumes with the PD streamline model. All conditions were assessed 3 months after surgery, and both clinical and streamline-informed DBS settings had been active for at least 24 h at the time of testing. The patient with PD was blinded to the DBS settings (clinically optimized versus streamline-informed) and evaluated by an independent physician blinded to the programming conditions. In the second reprogramming case of a patient with OCD from Boston receiving DBS to the VC/VS region, Y-BOCS scores were taken 1 month after surgery under clinical parameters as well as under parameters based on consideration of the OCD streamline model, and both conditions were compared to pre-surgical baseline. Of note, the patient was reprogrammed for clinical purposes, after clinically optimized stimulation parameters had failed to provide sufficient symptom relief. Thus, neither the patient nor the team of treating physicians was blinded to the activation of DBS nor to the programming condition (clinically optimized versus streamline-informed) during the evaluation of stimulation effects.

Third, the patient with OCD from the São Paulo center was treated via bilateral lead implantation surgery to the STN as well as stimulation parameter programming, which were both fully informed on the OCD streamline model. Y-BOCS outcome 1 month after streamline-based surgery and programming was finally contrasted to the severity of pre-operative OCD symptomatology. Given that only one condition was tested (streamline-optimized DBS), neither the evaluating physician nor the patient was blinded to the activation of DBS during the assessment.

In all three prospective patient cases, a pre-operative diffusion scan had been acquired, so that patient-specific tractography could be performed to confirm agreement between individual streamlines and normative connectivity models.

Dysfunction mappings at the level of indirect pathways

Besides hyperdirect fronto-cortical interconnections, the STN receives indirect projections from the striato-pallido-fugal system[29]. In second instance, we, thus, sought to understand whether and in which way indirect anatomical connections would be partitioned as a function of stimulation impact on disorder-wise core symptom domains. To this end, we appended an additional DBS Fiber Filtering analysis informed on pallido-subthalamic connections that had been extracted from the Basal Ganglia Pathway Atlas[26] while keeping remaining model parameters consistent.

Reporting summary

Further information on research design is available in the Nature Portfolio Reporting Summary linked to this article.

Data availability

Detailed patient-wise demographic and clinical information is available in Supplementary Tables 2–5, 7, 8 and 11 in anonymized form. Patient imaging data cannot be publicly shared as this would compromise patient privacy according to current data protection regulations. They are, however, available from the principal investigators of the collecting sites upon reasonable request within the framework of a data-sharing agreement. Inquiries for further information and data-sharing requests should be directed to the corresponding authors of this manuscript (A.H., ahorn1@bwh.harvard.edu, or N.L., ningfei.li@gmail.com) who commit to replying to any request within a timeframe of 30 d. Anonymized E-field derivatives along with pre- and postoperative clinical outcome scores of patients analyzed for the purpose of the present manuscript can be retrieved via a dedicated public repository, which is embedded within the Open Science Framework (https://osf.io/zu9c6/)[95]. The atlas of sweet streamline profiles and sweet spots of all four disorders is also included in this repository. In addition, this atlas is openly available within Lead-DBS software, version 3.0 (https://www.lead-dbs.org/). Although a processed version of the HCP 985 Connectome[21] can be requested from the corresponding authors, source data are freely accessible via the repository of the HCP (https://www.humanconnectome.org/study/hcp-young-adult/document/1200-subjects-data-release). Furthermore, the DBS Tractography Atlas, version 2.1, can be openly downloaded (https://github.com/netstim/DBS-Tractography-Atlas.git). The HCP-1,065 diffusion source data[85] used to inform this atlas can be openly accessed via DSI-Studio (https://brain.labsolver.org/hcp_template.html; fiber orientation maps at 1-mm resolution). The following normative resources have been made openly available by the original authors: the MGH 760 μm Connectome[67] (https://data-dryad.org/stash/dataset/doi:10.5061/dryad.nzs7h44q2) and the Basal Ganglia Pathway Atlas[26] (https://osf.io/mhd4z/). The PD-matched PPMI-85 connectome can be openly and publicly derived via the Lead-DBS knowledge base (https://www.lead-dbs.org/helpsupport/knowledge-base/atlasesresources/normative-connectomes/). Source data used for calculation of this connectome can be freely accessed via the homepage of the Parkinson's Progression Markers Initiative (https://www.ppmi-info.org/access-data-specimens/download-data). The OCD matched connectome can be shared by the corresponding authors upon reasonable request (see contact details stated above). Source data of patients with OCD employed to calculate this connectome cannot be publicly shared due to patient privacy restrictions. The DISTAL atlas, version 1.1 (ref. 28), and the CIT168 atlas, version 1.1 (ref. 69), are openly available via the Lead-DBS knowledge base (https://www.lead-dbs.org/helpsupport/knowledge-base/atlasesresources/atlases-2/) and come pre-installed with the Lead-DBS software. The JHU atlas parcellation[68] is openly accessible as a pre-installation within the Surf Ice software (https://www.nitrc.org/projects/surfice/).

Code availability

The entirety of code used in the analyses presented in this work is openly available within the Lead-DBS environment (https://github.com/leaddbs/leaddbs).

References

70. Treu, S. et al. Deep brain stimulation: imaging on a group level. *Neuroimage* **219**, 117018 (2020).
71. Faul, F., Erdfelder, E., Buchner, A. & Lang, A.-G. Statistical power analyses using G*Power 3. 1: tests for correlation and regression analyses. *Behav. Genet.* **41**, 1149–1160 (2009).
72. Faul, F., Erdfelder, E., Lang, A.-G. & Buchner, A. G*Power 3: a flexible statistical power analysis program for the social, behavioral, and biomedical sciences. *Behav. Res. Methods* **39**, 175–191 (2007).

73. Tyagi, H. et al. A randomized trial directly comparing ventral capsule and anteromedial subthalamic nucleus stimulation in obsessive-compulsive disorder: clinical and imaging evidence for dissociable effects. *Biol. Psychiatry* **85**, 726–734 (2019).

74. Neudorfer, C. et al. Lead-DBS v3.0: mapping deep brain stimulation effects to local anatomy and global networks. *Neuroimage* **268**, 119862 (2023).

75. Avants, B. B., Epstein, C. L., Grossman, M. & Gee, J. C. Symmetric diffeomorphic image registration with cross- correlation: evaluating automated labeling of elderly and neurodegenerative brain. *Med. Image Anal.* **12**, 26–41 (2008).

76. Fonov, V. et al. Unbiased average age-appropriate atlases for pediatric studies. *Neuroimage* **54**, 313–327 (2011).

77. Neudorfer, C. et al. Personalizing deep brain stimulation using advanced imaging sequences. *Ann. Neurol.* **91**, 613–628 (2022).

78. Horn, A. & Kühn, A. A. Lead-DBS: a toolbox for deep brain stimulation electrode localizations and visualizations. *Neuroimage* **107**, 127–135 (2015).

79. Vorwerk, J., Oostenveld, R., Piastra, M. C., Magyari, L. & Wolters, C. H. The FieldTrip-SimBio pipeline for EEG forward solutions. *Biomed. Eng. Online* **17**, 37 (2018).

80. Åström, M., Diczfalusy, E., Martens, H. & Wårdell, K. Relationship between neural activation and electric field distribution during deep brain stimulation. *IEEE Trans. Biomed. Eng.* **62**, 664–672 (2015).

81. Vasques, X. et al. Stereotactic model of the electrical distribution within the internal globus pallidus during deep brain stimulation. *J. Comput. Neurosci.* **26**, 109–118 (2009).

82. Horn, A. et al. Deep brain stimulation induced normalization of the human functional connectome in Parkinson's disease. *Brain* **142**, 3129–3143 (2019).

83. Jakab, A. et al. Feasibility of diffusion tractography for the reconstruction of intra-thalamic and cerebello-thalamic targets for functional neurosurgery: a multi-vendor pilot study in four subjects. *Front. Neuroanat.* **10**, 76 (2016).

84. Petersen, M. V. et al. Probabilistic versus deterministic tractography for delineation of the cortico-subthalamic hyperdirect pathway in patients with Parkinson disease selected for deep brain stimulation. *J. Neurosurg.* **126**, 1657–1668 (2017).

85. Yeh, F.-C. et al. Quantifying differences and similarities in whole-brain white matter architecture using local connectome fingerprints. *PLoS Comput. Biol.* **12**, e1005203 (2016).

86. Pijnenburg, R. et al. Myelo- and cytoarchitectonic microstructural and functional human cortical atlases reconstructed in common MRI space. *Neuroimage* **239**, 118274 (2021).

87. Yeh, F. C. et al. Automatic removal of false connections in diffusion MRI tractography using topology-informed pruning (TIP). *Neurotherapeutics* **16**, 52–58 (2019).

88. Riva-Posse, P. et al. A connectomic approach for subcallosal cingulate deep brain stimulation surgery: prospective targeting in treatment-resistant depression. *Mol. Psychiatry* **23**, 843–849 (2018).

89. Jenkinson, M., Beckmann, C. F., Behrens, T. E. J., Woolrich, M. W. & Smith, S. M. FSL. *Neuroimage* **62**, 782–790 (2012).

90. Yeh, F. C., Wedeen, V. J. & Tseng, W. Y. I. Generalized *q*-sampling imaging. *IEEE Trans. Med. Imaging* **29**, 1626–1635 (2010).

91. Marek, K. et al. The Parkinson Progression Marker Initiative (PPMI). *Prog. Neurobiol.* **95**, 629–635 (2011).

92. Ashburner, J. A fast diffeomorphic image registration algorithm. *Neuroimage* **38**, 95–113 (2007).

93. Horn, A., Ostwald, D., Reisert, M. & Blankenburg, F. The structural–functional connectome and the default mode network of the human brain. *Neuroimage* **102**, 142–151 (2014).

94. Horn, A. & Blankenburg, F. Toward a standardized structural–functional group connectome in MNI space. *Neuroimage* **124**, 310–322 (2016).

95. Li, N., Hollunder, B., & Horn, A. DBS dysfunctional circuits *Open Science Framework* https://doi.org/10.1038/s41593-024-01570-1 (2024).

Acknowledgements

Author contributions

B.H.: conceptualization, data curation, methodology, formal analysis, visualization, writing—original draft and funding acquisition. J.L.O., M.P., H.A., M.V., C. Z., B.S., J.C.B., T.A.D., V.V.-V., J.V., A.A.K., A.M., L.M.R., H.T., L.Z., E.M.J., S.C. and P.A.S.: resources, data curation and writing—review and editing. I.A.S.: data curation, formal analysis and writing—review and editing. N.R.: methodology, software, resources, data curation and writing—review and editing. S.O.: methodology, software, formal analysis, software and writing—review and editing. K.B.: methodology, software, formal analysis, data curation and writing—review and editing. C.N.: investigation, visualization and writing—review and editing. P.R.: methodology, formal analysis and writing—review and editing. P.Z.: visualization, data curation, formal analysis and writing—review and editing. P. Navratil, M.M.R., E.J.L.A. and P.R.F.: investigation, resources, data curation and writing—review and editing. F.-C.Y.: methodology, software and writing—review and editing. C.F., H.B. and M.R.D.: writing—review and editing. P. Nanda: investigation and writing—review and editing. D.D.D. and R.M.R.: investigation, resources, data curation and writing—review and editing. N.L. and A.H.: conceptualization, methodology, software, formal analysis, resources, data curation, writing—original draft, visualization, supervision, project administration and funding acquisition.

Competing interests

Additional information

Supplementary information The online version contains supplementary material available at https://doi.org/10.1038/s41593-024-01570-1.

Correspondence and requests for materials should be addressed to Ningfei Li or Andreas Horn.

Peer review information *Nature Neuroscience* thanks Pierre-Louis Bazin, Evan Gordon and Casey Halpern for their contribution to the peer review of this work.

Reprints and permissions information is available at www.nature.com/reprints.

nature portfolio

Corresponding author(s):   Andreas Horn, MD PhD; Ningfei Li, PhD

Last updated by author(s):   01/26/2024

Reporting Summary

Nature Portfolio wishes to improve the reproducibility of the work that we publish. This form provides structure for consistency and transparency in reporting. For further information on Nature Portfolio policies, see our Editorial Policies and the Editorial Policy Checklist.

Statistics

For all statistical analyses, confirm that the following items are present in the figure legend, table legend, main text, or Methods section.

n/a	Confirmed	
☐	☒	The exact sample size (n) for each experimental group/condition, given as a discrete number and unit of measurement
☐	☒	A statement on whether measurements were taken from distinct samples or whether the same sample was measured repeatedly
☐	☒	The statistical test(s) used AND whether they are one- or two-sided *Only common tests should be described solely by name; describe more complex techniques in the Methods section.*
☒	☐	A description of all covariates tested
☐	☒	A description of any assumptions or corrections, such as tests of normality and adjustment for multiple comparisons
☐	☒	A full description of the statistical parameters including central tendency (e.g. means) or other basic estimates (e.g. regression coefficient) AND variation (e.g. standard deviation) or associated estimates of uncertainty (e.g. confidence intervals)
☐	☒	For null hypothesis testing, the test statistic (e.g. F, t, r) with confidence intervals, effect sizes, degrees of freedom and P value noted *Give P values as exact values whenever suitable.*
☒	☐	For Bayesian analysis, information on the choice of priors and Markov chain Monte Carlo settings
☒	☐	For hierarchical and complex designs, identification of the appropriate level for tests and full reporting of outcomes
☐	☒	Estimates of effect sizes (e.g. Cohen's d, Pearson's r), indicating how they were calculated

Our web collection on statistics for biologists contains articles on many of the points above.

Software and code

Policy information about availability of computer code

Data collection   Clinical outcome data and deep brain stimulation (DBS) parameters were retrieved from the collecting sites using Microsoft Excel v16.70 and imported for analysis via MATLAB R2022b, v9.13.0.2105380. Optimal DBS streamline profiles and sweet spots were constructed using MATLAB scripts (openly available within the Lead-DBS environment, https://www.lead-dbs.org/), the former combined with public human connectome data, see prior studies based on the same approach (e.g., Baldermann et al., 2019, Biol. Psychiatry; Horn et al., 2022, Proc. Natl. Acad. Sci; Irmen et al., 2020, Ann. Neurol.).

Data analysis   All statistical analyses were conducted using MATLAB scripts openly and publicly available within the Lead-DBS environment (https://www.lead-dbs.org/): https://github.com/netstim/leaddbs

As described in the manuscript, all analysis approaches built upon Lead-DBS, v3.0 software and included preprocessing of patient-specific imaging (head CT/MRI), followed by electrode reconstruction (both via the Lead-DBS toolbox) as well as estimation of stimulation volumes (via the Lead-Group toolbox). Some of these processig steps build upon algorithms adapted from SPM12, Advanced Normalization Tools (ANTs), Precise and Convenient Electrode Reconstruction for Deep Brain Stimulation (PaCER), SimBio, or FieldTrip (see https://www.lead-dbs.org/about/lead-dbs-dependencies/). The Symmetric Normalization (SyN) approach included in ANTs, as pre-installed with Lead-DBS, v3.0, was used for multispectral spatial normalization into template space. Manual optimizations of the standard normalization warp-fields were based on the WarpDrive toolbox, as implemented in Lead-DBS, v3.0 (https://github.com/netstim/SlicerNetstim). Electrodes were pre-localized using the PaCER algorithm, or the trajectory search/contact reconstructions (TRAC/CORE) algorithm, both as pre-installed with Lead-DBS, v3.0 software. The electric field (E-field) was simulated via an adaptation of the SimBio/FieldTrip pipeline (https://www.mrt.uni-jena.de/simbio/; http://fieldtriptoolbox.org/), as implemented in Lead-DBS, v3.0 software. G*Power software, v 3.1.9.6 was used to determine the power to detect a presumed effect by means of our available sample sizes.

Based on Lead-DBS-internal toolboxes, patient-specific results were further processed at the group-level using DBS Sweet Spot Mapping (via the DBS Sweet Spot Mapping Explorer) and DBS Fiber Filtering (via the DBS Fiber Filtering Explorer), both as included in Lead-DBS, v3.0.

SPM12 (https://www.fil.ion.ucl.ac.uk/spm/) was used for smoothing of sweet spots and sweet streamline bundles converted to voxelized images (tract-density maps). Surf Ice software, v.1.0.20211006 (https://www.nitrc.org/projects/surfice; https://github.com/neurolabusc/surf-ice/releases) was applied to display the topographical organization of sweet spots and that of interconnected sites of sweet streamlines at the cortical level in three-dimensional space. Finally, disease-wise sweet in conjunction with sour spots were displayed individually using 3D Slicer software, v5.2.1 (https://www.slicer.org/).

Diffusion-weighted magnetic resonance imaging (dMRI) data used to create the OCD disease matched connectome were preprocessed via FMRIB Software Library (FSL), Release 6.0 (https://fsl.fmrib.ox.ac.uk/fsl/fslwiki/FSL). DSI-Studio (http://dsi-studio.labsolver.org/) was employed to construct the OCD matched connectome, as well as the DBS Tractography atlas, v2.1, which served the purpose of informing connectivity-based analyses in the present study (amongst other previously established connectomic resources).

For manuscripts utilizing custom algorithms or software that are central to the research but not yet described in published literature, software must be made available to editors and reviewers. We strongly encourage code deposition in a community repository (e.g. GitHub). See the Nature Portfolio guidelines for submitting code & software for further information.

Data

Policy information about availability of data

All manuscripts must include a data availability statement. This statement should provide the following information, where applicable:
- Accession codes, unique identifiers, or web links for publicly available datasets
- A description of any restrictions on data availability
- For clinical datasets or third party data, please ensure that the statement adheres to our policy

Patient-specific data:
The analyses described in this manuscript build on datasets of eleven patient cohorts and three prospective patient cases from a total of ten international institutions. Detailed patient-wise demographic and clinical information is available in the supplementary materials in anonymized form. Imaging data cannot be publicly shared due to patient privacy restrictions but is available from the principal investigators of the collecting sites upon reasonable request within the scope of a data sharing agreement. Inquiries for further information and data sharing requests should be directed to the corresponding authors of this manuscript (A.H., via ahorn1@bwh.harvard.edu, or N.L., via ningfei.li@gmail.com) who commit to replying to any request within a timeframe of 30 days. Anonymized E-fields of patients analyzed in this work are made publicly available alongside clinical outcome information via a dedicated open repository of the Open Science Framework (OSF) (https://osf.io/zu9c6/).

Atlas of results:
The sweet streamline and sweet spot profiles are openly available in the form of an atlas included within Lead-DBS software, v3.0 (https://www.lead-dbs.org), as well as from the above-mentioned public repository of the OSF associated with this study (https://osf.io/zu9c6/).

Normative data:
- Human Connectome Project (HCP) 985 Connectome: The processed version (as described in Li et al., 2020, Nat. Commun) is currently not openly available but can be shared by the corresponding authors upon reasonable request. Source data used to calculate this connectome are openly accessible via the repository of the HCP (https://www.humanconnectome.org/study/hcp-young-adult/document/1200-subjects-data-release).
- Massachusetts General Hospital 760 μm Connectome (Edlow et al., 2019, Sci. Data): openly available from https://datadryad.org/stash/dataset/doi:10.5061/dryad.nzs7h44q2
- Basal Ganglia Pathway Atlas (Petersen et al., 2019, Neuron): openly available from https://osf.io/mhd4z/
- DBS Tractography Atlas, v2.1: The processed version of this atlas resource is openly available (https://github.com/netstim/DBS-Tractography-Atlas.git). The HCP-1,065 diffusion source data used to inform this pathway atlas can be openly accessed via DSI-Studio (https://sites.google.com/a/labsolver.org/brain/diffusion-mri-data/hcp-dmri-data).
- Parkinson's Progression Marker Initiative (PPMI)-85 Connectome, v1.1 (Ewert et al., 2018): The processed version can be openly and publicly derived via the Lead-DBS knowledge base (https://www.lead-dbs.org/helpsupport/knowledge-base/atlasesresources/normative-connectomes/). Source data used for calculation of this connectome can be freely accessed via the homepage of the PPMI (https://www.ppmi-info.org/access-data-specimens/download-data).
- OCD-06 Connectome: The processed version of this connectome can be shared by the corresponding authors upon reasonable request. Source data of OCD patients employed to calculate this connectome cannot be publicly shared due to patient privacy restrictions but is available from the principal investigators of the collecting sites upon reasonable request within the scope of a data sharing agreement. Inquiries for further information and data sharing requests should be directed to the corresponding authors of this manuscript (A.H., via ahorn1@bwh.harvard.edu, or N.L., via ningfei.li@gmail.com) who commit to replying to any request within a timeframe of 30 days.

Cortical and subcortical atlases:
- DBS Intrinsic Template (DISTAL) atlas, v1.1 (Ewert et al., 2017): The atlas is openly available via the Lead-DBS knowledge base (https://www.lead-dbs.org/helpsupport/knowledge-base/atlasesresources/atlases-2/) and comes pre-installed with the Lead-DBS software package.
- Johns Hopkins University (JHU) atlas parcellation (Faria et al., 2012): The atlas is openly accessible as a pre-installation within the Surf Ice software (https://www.nitrc.org/projects/surfice/).
- California Institute of Technology reinforcement learning atlas, v1.1 (CIT168; Pauli et al., 2018): The atlas is openly available via the Lead-DBS knowledge base (https://www.lead-dbs.org/helpsupport/knowledge-base/atlasesresources/atlases-2/) and comes pre-installed with the Lead-DBS software package.

Human research participants

Policy information about studies involving human research participants and Sex and Gender in Research.

Reporting on sex and gender   Proportions of self-identified gender in the sample are reported in the manuscript (Tables S1-8 & S11). No statistical analyses

Reporting on sex and gender	with regard to gender- or sex-specific groups have been performed as no differences relevant to the research question in focus were to be expected.

Population characteristics	Discovery cohorts: Sweet spot and sweet streamline models were created based on data from eight international cohorts of bilaterally implanted DBS patients (N = 197, 394 DBS electrodes) receiving stimulation to the subthalamic region for treatment of one of four different brain disorders: dystonia (DYT; n = 70, 38 females), Parkinson's disease (PD; n = 94, 29 females), obsessive-compulsive disorder (OCD; n = 19, 10 females), and Tourette's syndrome (TS; n = 14, 3 females). Please refer to tables S1-5 for detailed and comprehensive group-level as well as patient-wise information on relevant demographic and clinical patient characteristics. Retrospective validation cohorts: PD and OCD streamline models were retrospectively validated based on an additional cohort of patients each. The validation cohort of PD patients (n = 32, 10 females) had been implanted to the subthalamic nucleus (STN), while OCD patients (n = 35, 18 female) received DBS to the ventral capsule/ventral striatum (VC/VS) region. Tables S6-8 comprise detailed cohort-averaged and patient-specific demographic and clinical information. Prospective patient cases: Two DBS patients (one with PD and OCD each) were prospectively reprogrammed and one additional patient with OCD was prospectively implanted and programmed based on the respectively corresponding streamline models. The first prospective reprogramming case comprised a 67-year-old male patient with PD receiving DBS targeted to the STN, and the second case a 21-year-old female patient with OCD implanted to the VC/VS region. The surgical case was a 32-year-old male patient with OCD receiving STN-DBS. Table S11 lists more detailed patient-specific information on these three patient cases.
Recruitment	Retrospectice data: Each dataset relied on different recruitment parameters depending on the respective study type (as listed in Tables S1 & S6). Further details on recruitment procedures are either described in our previous publications, i.e., Horn et al., 2017, Ann. Neurol & Horn et al., 2019, Brain (PD cohorts from Berlin and Würzburg), or in the original source publication(s) by each respective collecting site. These latter comprised studies by Dai et al., 2022, J. Neurol. (TS discovery cohort from Shanghai), Vissani et al. (2019), J. Neural Eng. (TS discovery cohort from Pisa/Milan), Tyagi et al., 2019, Biol. Psychiatry (OCD discovery and model validation cohort from London), Polosan et al. (2019), Transl. Psychiatry (OCD discovery cohort from Grenoble), Lin et al., 2019, J. Neurosurg. & He et al., 2021, Front. Neurol. (DYT discovery cohort from Shanghai), Ostrem et al., 2011 & 2016, Neurology (DYT disovery cohort from San Francisco), Butenko et al., 2022, NeuroImage Clin. (model validation cohort from Würzburg), McLaughlin et al., 2021, Contemp. Clin. Trials Commun. (model validation cohort from Boston), as well as Baldermann et al., 2019, Biol. Psychiatry & Li et al., 2020, Nat. Commun. (model validation cohort from Cologne). Prospective patient cases: -PD reprogramming case from Würzburg, Germany: The PD patient from Würzburg was investigated within the ongoing clinical service of the inpatient DBS program at University Hospital Würzburg. Reprogramming took place based on a multidisciplinary assessment of DBS location and streamline information. -OCD reprogramming case from Boston, MA, USA: This patient was investigated within the ongoing clinical service of the DBS program at Massachusetts General Hospital (MGH; psychiatry and neurosurgery departments). Reprogramming for clinical purposes took place based on a multidisciplinary assessment of DBS location and streamline information. -OCD-DBS implantation case from São Paulo, Brazil: This patient was recruited within the regular surgical service of Clínica de Dor e Funcional after classification as a refractory case of OCD, associated with depression. He underwent evaluation by a neurologist, psychologist and two functional neurosurgeons prior to the analysis of the Ethics Board Commite of the State of Rio Grande do Sul, who finally aproved the DBS surgery proposed by the team.
Ethics oversight	This research complied with all relevant ethical regulations and post-hoc analyses were approved by the institutional review board at Charité – Universitätsmedizin (Berlin, Germany; master vote EA2/186/18). Procedures of clinical trials and studies leading to the collection of the herein analyzed data were approved by the individual institutional review boards at each of the respective collecting sites (DBS centers in San Francisco, Shanghai, Pisa/Milan, London, Grenoble, Berlin, Würzburg, Boston, & Cologne). They were all carried out in accord with the declaration of Helsinki from 1975, and all participants signed an informed consent prior to study participation. Participants received no compensation in exchange for their participation in the trials and studies.

Note that full information on the approval of the study protocol must also be provided in the manuscript.

Field-specific reporting

Please select the one below that is the best fit for your research. If you are not sure, read the appropriate sections before making your selection.

☒ Life sciences ☐ Behavioural & social sciences ☐ Ecological, evolutionary & environmental sciences

For a reference copy of the document with all sections, see nature.com/documents/nr-reporting-summary-flat.pdf

Life sciences study design

All studies must disclose on these points even when the disclosure is negative.

Sample size	Since neuropsychiatric disorders represent comparably recent and rare applications of DBS to the STN target, available samples – especially in TS and OCD – are largely restricted by the small number of surgeries performed world-wide to date. In the TS cohort, we included the full

number of patients stimulated to the STN in this disease globally available at the time of analyses. Overall, we were able to identify two independent datasets in all four disorders for the model set-up (discovery cohorts) that linked DBS sites to improvements in respective primary clinical outcome.

Given the exploratory nature of our study, an a priori power analysis was not straight-forward. Our initial assumption of expected effect sizes was based on Li et al., 2020, Nat. Commun, and Treu et al. 2020, Neuroimage, with an r of approximately 0.4 for reported correlations between empirical clinical outcomes and estimated gain scores. Given the natural restrictions in available sample sizes described above, we calculated a "compromise" type power analysis using G*Power, v 3.1.9.6 (Faul et al., 2007; 2009, Behav. Res. Methods) to determine the power of our analysis based on the accessible data per disorder to detect the assumed effect. Given a β/α ratio of 1, the available DYT sample (n = 56 in the main cohort) used for model set-up was powered to 0.94 (implied α/β error probability = 0.06), the PD sample (n = 94) to 0.98 (implied α/β error probability = 0.02), the TS sample (n = 14) to 0.77 (implied α/β error probability = 0.23), and the OCD sample (n = 19) to 0.81 (implied α/β error probability = 0.19) for detecting the assumed effect size.

In additon, we performed a total of five validation experiments based on data unseen by the models, featuring two retrospective patient cohorts, one comprised of patients with PD (N = 32) and one of patients with OCD (N = 35, spanning three institutions) as well as three prospective patient cases. To our knowledge, this is the largest transdiagnostic study of its kind.

Data exclusions	All participants with complete neuroimaging and clinical outcome scores in the respective primary assessment were included in our analyses.
Replication	We assessed overall reproducibility of sweet spot and sweet streamline profiles in their ability of explaining clinical improvements in hold-out data using a five-fold cross-validation design, across two independent datasets per disease type from a total of seven institutions. Additionally, the main study result (i.e., the topographical organization of sweet streamlines) was re-assessed in four normative and two disease-matched connectomic resources of different properties to scrutinize the influence of choice of a specific tractogram. These additional analyses revealed a largely similar organizational pattern of dysfunction mappings irrespective of which connectome the attributions had been informed on. Moreover, streamline models in two exemplary disorders (OCD and PD) were retrospectively validated in independent (out-of-sample) data of one additional patient cohort each (with the OCD validation sample spanning data pooled across three institutions).
Randomization	Our study compared optimal connectivity and focal stimulation sites associated with symptom improvement in relation to precisely placed DBS electrodes between four different disease cohorts. Group affiliation of patients was thus determined by disorder category. This approach did not involve any form of experimental manipulation, comparison of conditions, or stimulus presentation, and the majority of results (with the exception of the three prospective patient cases for model validation) were based on retrospective data analysis. Instead of prospective randomization, we leveraged incidental variability in electrode placement within each disease-cohort, which can be presumed to be random.
Blinding	Secondary analysis of retrospective data: Blinding was not relevant for the main body of our study which consisted of a secondary analysis of existing datasets. To minimize the risk of observer bias, we tested the explanatory value of both DBS sweet spot and sweet streamline profiles for clinical outcome variability within the respective clinical outcome measure in hold-out data in a five-fold cross-validation design (and across connectomic resources, in the case of streamline profiles). We additionally performed retrospective model validations based on two additional independent datasets of two of the investigated disorders (OCD and PD). Prospective patient cases: -PD reprogramming case from Würzburg, Germany: The patient was blinded to the DBS settings (clinically optimized vs. streamline-informed) and evaluated by an independent physician blind to the programming conditions. -OCD reprogramming case from Boston, MA, USA: The patient was reprogrammed for clinical purposes, after clinically optimized stimulation parameters had failed to provide symptom relief. Thus, neither the patient nor the team of treating physicians was blinded to the activation of DBS nor to the programming condition (clinically optimized vs. streamline-informed) during the postsurgical evaluation of stimulation effects. -OCD-DBS implantation case from São Paulo, Brazil: Given that only one condition was tested (streamline-optimized DBS), neither the patient nor the team of treating physicians was blinded to the activation of DBS during the postsurgical evaluation of stimulation effects.

Reporting for specific materials, systems and methods

We require information from authors about some types of materials, experimental systems and methods used in many studies. Here, indicate whether each material, system or method listed is relevant to your study. If you are not sure if a list item applies to your research, read the appropriate section before selecting a response.

Materials & experimental systems

n/a	Involved in the study
☒	Antibodies
☒	Eukaryotic cell lines
☒	Palaeontology and archaeology
☒	Animals and other organisms
☒	Clinical data
☒	Dual use research of concern

Methods

n/a	Involved in the study
☒	ChIP-seq
☒	Flow cytometry
☐	☒ MRI-based neuroimaging

Magnetic resonance imaging

Experimental design

Design type	Individualized structural MRI and/or CT of the head combined with normative structural human connectome data
Design specifications	Patient-specific structural MRI or CT scans of the head were used to localize stimulation sites (Horn & Kühn, 2014, Neuroimage; Horn et al., 2019, Neuroimage; Neudorfer et al., 2023, Neuroimage). Accounting for individual stimulation parameters, E-fields were further calculated to measure the stimulation impact on surrounding anatomy. Based on these patient-specific electrode localizations and stimulation volumes, analysis (1) relied on voxel-wise weighting of the stimulation effect by its impact on clinical outcomes in each disorder-wise primary clinical outcome measure using DBS Sweet Spot Mapping (Horn et al., 2022, Proc. Natl. Acad. Sci; Neudorfer et al., 2023, Neuroimage). In analysis (2), six different normative human connectomes (four healthy & two disease-matched) were employed to estimate clinically relevant structural connectivity across stimulation volumes using DBS Fiber Filtering (Baldermann et al., 2019, Biol. Psychiatry; Irmen et al., 2020, Ann. Neurol.; Neudorfer et al., 2023, Neuroimage). The main connectomic resource employed to inform analysis part (2) consisted of a group connectome representative of average connectivity in a large healthy human sample (n = 985) (Li et al., 2020, Nat. Commun) from the HCP (Van Essen et al., 2013, Neuroimage). Analyses were further repeated using a normative ultra-high-resolution (760 µm isotropic) tractogram of a single healthy participant (Edlow et al., 2019, Sci. Data), the Basal Ganglia Pathway Atlas (Petersen et al., 2019, Neuron), as well as a customized pathway atlas (DBS Tractography Atlas, v2.1) explicitly created for this work using population-based fiber tracking and expert-defined pathways with focus on cortico-subthalamic inputs not represented in other atlas resources (for a detailed description of the creation of this atlas resource, please see the methods section in the main manuscript). Finally, two disease-matched connectomes were implemented to scrutinize the generalizability of dysfunction mappings in the face of disease-specific connectivity alterations on the examples of PD and OCD. The former comprised the PPMI-85 Connectome (Ewert et al., 2018, NeuroImage) and the latter the OCD-06 Connectome which had been calculated for the purpose of the present study based on diffusion imaging data by n = 6 patients with OCD.
Behavioral performance measures	Datasets used disorder-specific scales to measure primary clinical outcomes (as delineated in Tables S1 & S6). These comprised the Burke-Fahn-Marsden Dystonia Rating Scale (BFMDRS) in DYT, the Unified Parkinson's Disease Rating Scale – Part III (motor part; UPDRS-III) in PD, the Yale Global Tic Severity Scale (YGTSS) in TS, and the Yale-Brown Obsessive-Compulsive Scale (Y-BOCS) in OCD. Stimulation-related change within these measures relative to baseline (pre- vs. postoperative under DBS ON, or postoperative DBS OFF vs. ON conditions in the case of PD) was related to voxels in the subthalamic zone (DBS Sweet Spot Mapping) or structural connectivity (DBS Fiber Filtering).

Acquisition

Imaging type(s)	Normative dMRI data of n = 985 healthy controls from the HCP 1,200 subjects release (Van Essen et al., 2013, NeuroImage) for the construction of the HCP 985 Connectome, of n = 1,065 healthy young adults (Yeh et al., 2016, PLoS Comput. Biol.) for the construction of the DBS Tractography Atlas, v2.1 (see Methods for details on the creation of this atlas resource), of n = 85 Parkinson's disease patients from the PPMI (Marek et al., 2011, Prog. Neurobiol.), of n = 6 OCD patients (Tyagi et al., 2019, Biol. Psychiatry), as well as individualized (patient-specific) preoperative structural MRI (n = 261) and postoperative MRI (n = 73) or CT of the head (n = 188).
Field strength	MRI data collected using 3T scanner
Sequence & imaging parameters	Preoperative T1 & T2-weighted MRI, postoperative T1-weighted MRI (n = 73) or CT (n= 188) of the head; each dataset used different structural imaging parameters, as described in the respective source publications (see Tables S1 & S6)
Area of acquisition	Whole brain

Diffusion MRI   ☒ Used   ☐ Not used

Parameters	-HCP data (see Van Essen et al., 2013, NeuroImage, for details): The gradient table included approximately 90 diffusion weighting directions plus 6 b = 0 acquisitions interpersed throughout each run. Diffusion weigthing consisted of 3 shells of b = 1000, 200, or 3000 s/mm^2 interpersed with an approximately equal numbr of acquisitions on each shell within each run. -PPMI data (see Marek et al., 2011, Prog. Neurobiol., for details): Acquisition was performed along 64 uniformly distributed directions with b = 1000 s/mm^2 and a single b = 0 image. A single shot echo-planar imaging (EPI) sequence (116 × 116 matrix, 2 mm isotropic resolution, TR/TE = 900/88 ms, two-fold acceleration) was implemented. -OCD data (see Tyagi et al., 2019, Biol. Psychiatry, for details): Diffusion-weighting was applied with b = 1500 s/mm^2 along 128 directions uniformly distributed on the sphere and seven b = 0s volumes were acquired. For distortion correction a reversed phase encoding direction was applied for all acquisitions (resulting in 270 volumes in total).

Preprocessing

Preprocessing software	MATLAB-based Lead-DBS software, v3.0 (Neudorfer et al., 2023, Neuroimage) was used for preprocessing, including toolbox-internal dependencies on SPM12 and ANTs: https://github.com/netstim/leaddbs

Normalization	Multispectral spatial normalization using the SyN approach included in ANTs (http://stnava.github.io/ANTs/) with the 'Effective: low variance + subcortical refinement' preset in Lead-DBS, v3; normalization warp-fields were further visually inspected and manually optimized using the WarpDrive tool as included in Lead-DBS (Oxenford et al., 2023, MedIA), if needed, with particular attention to the STN as the anatomical structure in focus.
Normalization template	ICBM 2009b NLIN Asymmetric non-linear 2009b MNI152
Noise and artifact removal	Biasfield correction; correction for potential intraoperative brain shift via an automatized subcortical refinement module (as implemented in Lead-DBS, v3)
Volume censoring	Volume censoring is a motion denoising method used for functional MRI (fMRI) images. Since no fMRI data was analyzed in this study, volume censoring was not applied.

Statistical modeling & inference

Model type and settings	Mass-univariate analysis based on an in-sample spatial Spearman's correlation and subsequent validation of explanatory value of sweet spot and sweet streamline profiles for clinical outcome variability in a five-fold cross-validation design across two independent data sets per disease category; specificity analysis to test the predictive utility of disease-wise sweet streamline models for clinical outcome in all remaining three disorders; additional retrospective validation of the capability of streamline models to account for clinical outcome variance in independent (out-of-sample) patient cohorts
Effect(s) tested	Correlation between stimulation site connectivity (in the case of DBS Fiber Filtering) or activated voxels (in the case of DBS Sweet Spot Mapping) and change in pre- to post-treatment severity (or change in severity under postoperative ON vs. OFF DBS conditions in the case of PD) within the respective primary clinical outcome scale: BFMDRS in DYT, UPDRS-III (motor part) in PD, YGTSS in TS, and Y-BOCS in OCD

Specify type of analysis: ☒ Whole brain   ☐ ROI-based   ☐ Both

Statistic type for inference (See Eklund et al. 2016)	Voxel-wise
Correction	Validation of the generalizability of mass-univariate results in hold-out data using five-fold cross-validation and in six different connectomic resources (in the case of DBS Fiber Filtering results); model validation based on independent (out-of-sample) data of additional patient cohorts

Models & analysis

n/a	Involved in the study
☒ ☐	Functional and/or effective connectivity
☒ ☐	Graph analysis
☒ ☐	Multivariate modeling or predictive analysis